Tissue-scale mechanics controls differentiation strategy and dynamics of epithelial multilayering

Clémentine Villeneuve[1, 2]*, Somiealo Azote Epse Hassikpezi [3]*, Marga Albu[2], Matthias Rübsam[4], Leah C. Biggs[1,2], Sabrina Vinzens[2], Kai Kruse[5], Anubhav Prakash[2], Peter Zentis[6], Elizabeth Lawson-Keister[3], Gautier Follain[7,8,9], Johanna Ivaska[7,10,11], Carien M. Niessen[4§], M. Lisa Manning[3§], and Sara A. Wickström[1,2,12§]

[1]Stem Cells and Metabolism Research Program, Faculty of Medicine, University of Helsinki, 00290 Helsinki Finland

[2]Department of Cell and Tissue Dynamics, Max Planck Institute for Molecular Biomedicine, 48149 Münster, Germany

[3]Department of Physics and BioInspired Institute, Syracuse University, Syracuse, NY, USA.

[4]Department Cell Biology of the Skin, Cologne Excellence Cluster on Cellular Stress Responses in Aging Associated Diseases (CECAD), Center for Molecular Medicine Cologne, University Hospital Cologne, University of Cologne, Joseph-Stelzmann-Str. 26, 50931 Cologne, Germany.

[5]Max Planck Institute for Molecular Biomedicine, 48149 Münster, Germany

[6]Cluster of Excellence for Aging-Associated Diseases, CECAD Imaging Facility Cologne, University of Cologne, Cologne, Germany.

[7]Turku Bioscience Centre, University of Turku and Åbo Akademi University, Turku, 20520, Finland

[8]Faculty of Science and Engineering, Cell Biology, Åbo Akademi University, Turku, 20520, Finland

[9]Turku Collegium for Science, Medicine and Technology (TCSMT), Turku, 20520, Finland

[10]Department of Life Technologies, University of Turku, FI-20520 Turku, Finland.

[11]InFLAMES Research Flagship Center, University of Turku, Turku, Finland.

[12]Helsinki Institute of Life Science, Biomedicum Helsinki, University of Helsinki, FI-00290 Helsinki, Finland

*These authors contributed equally

[§]These authors jointly supervised this work

carien.niessen@uni-koeln.de

mmanning@syr.edu

sara.wickstrom@mpi-muenster.mpg.de

Abstract

Generating and maintaining multilayered epithelia requires coordinated cell division, differentiation, and tissue architecture, yet the precise mechanisms of multilayering remain unclear. Using the developing mouse epidermis, we show that basal stem cells adopt distinct multilayering strategies depending on tissue mechanics. Combining quantitative morphometry, embryo live imaging and physical modeling, we observe that early in development, the epidermis is fluid-like, allowing undifferentiated cells to move suprabasally through perpendicular divisions or basal detachment before differentiating. As the tissue matures and rigidifies, a mechanical barrier is established that only allows upward movement of basal cells that have committed to differentiation. The final step of this commitment is delamination that requires Notch signaling, triggered by increased tissue stiffness and jamming. This mechanical regulation orchestrates a feedback loop that induces cell upward motion precisely when the basal layer becomes crowded. Together, our findings identify tissue mechanics as the key determinant of how tissues drive multilayering and reveal mechanically regulated Notch signaling as a driver of epidermal delamination.

Introduction

Stratified epithelia such as the skin epidermis are multilayered tissues where the basal layer consists of undifferentiated epithelial stem cells adhering to the basement membrane, while the suprabasal layers contain post-mitotic, differentiated cells [1-3]. Unlike other dynamically self-renewing epithelia such as the intestine, in which clear tissue-scale geometric cues such as curvature compartmentalize the stem cell away from differentiated progeny [4], it remains unclear how stratified epithelia establish and organize this spatial organization and differentiation dynamics during development and into adulthood.

To initiate or maintain epidermal stratification, the basal stem cells generate suprabasal cells via two distinct strategies: perpendicular divisions or detachment from the basal layer, termed delamination [2,3,5]. Early in development, proliferation rates in the epidermis are high - to match the rapid growth of the organism it covers, and to generate sufficient suprabasal cells for efficient establishment of a functional life-essential barrier [6]. During this period, perpendicular cell divisions generate suprabasal daughter cells [7,8], while also some delaminations are observed [9,10]. In contrast, during adult homeostasis differentiation does not depend on cell divisions, with cells moving suprabasally exclusively through delamination to replenish the most superficial, desquamating cornified layers, followed by parallel divisions to maintain basal cell density [11,12]. Key open questions remain: Why

61 does this switch in strategies occur? And how is upward movement robustly regulated in the absence
62 of obvious niche inputs like tissue curvature?

63 Here we demonstrate that multilayering strategy is controlled by a mechanical barrier that is
64 established during development and hinders basal cells from moving upward. We establish a new
65 approach to quantitively measure this mechanical barrier by combining a 3D biophysical model for
66 cell and tissue mechanics with imaging of cell and tissue geometries in the basal layer and at the
67 basal-suprabasal interface. We find that at early developmental stages, embryonic (E) day 13.5/14.5,
68 there is little mechanical distinction between basal and suprabasal layers allowing basal cells to easily
69 place cells suprabasally either through perpendicular division or through rapid detachment assisted
70 by fluctuations from cell divisions. Around E15.5, a mechanical boundary between the basal and
71 suprabasal layers emerges, and basal cells must now undergo profound transcriptional
72 reprogramming– e.g., commit to delamination – in order to cross this boundary. How is this decision
73 to commit regulated? Our data suggests an elegant feedback mechanism involving Notch signaling.
74 Tissue crowding and stiffening trigger a transient Notch signal in a small subset of cells, causing
75 these cells to execute a transcriptional switch to complete delamination. Collectively, our study
76 shows that changes in tissue mechanics that drive intercompartment boundary formation are essential
77 determinants for a switch from early embryonic to a mature differentiation and multilayering
78 strategy. Moreover, we identify Notch signaling as an integrative feedback relay to precisely time the
79 transition between the mechanically separated basal and suprabasal compartments within the mature
80 stratified epithelium.

81

82 **Results**

83 **Basal cells employ distinct embryonic stage-specific strategies to generate and**
84 **compartmentalize suprabasal layers**

85 To understand which mechanisms are used for epidermal multilayering, we employed a whole
86 embryo live imaging system [9,13] to visualize long term (over 8 h) cell dynamics at E14.5 and E15.5
87 (Fig. 1A). While perpendicular divisions were prevalent at E14.5 as previously reported [8], parallel
88 oriented cell divisions became predominant at E15.5 with the overall frequency of cell divisions
89 decreasing (Fig. 1B). As reported [6], cell divisions also occurred suprabasally at E14.5 but much less
90 at E15.5 (Fig. 1B, Supplementary Fig. 1A). Imaging of fixed tissues showed that significantly more
91 undifferentiated cells were found in the first suprabasal layer at E14.5 than at E15.5 (Supplementary
92 Fig. 1B), as detected by the absence of the differentiation marker Keratin (K)10 [14] in suprabasal cells.

93 A fraction of these suprabasal undifferentiated cells were still proliferating at E14.5 but not at E15.5
94 (Fig. 1C). This suggested that differentiation is not associated with upward movement at early stages.

95 We then asked whether cell delamination dynamics also changed as a function of developmental
96 stage. At E14.5, detachment of cells from the basement membrane was regularly observed, with
97 upward movement lasting around 120 minutes. This detachment was frequently associated with a cell
98 division, either occurring after a perpendicular division or followed by a mitosis in the suprabasal
99 layer (Fig. 1D; Supplementary Movie 1). In contrast, at E15.5 delaminations were substantially
100 slower, lasting at least 300 minutes, and were not associated with divisions (Fig. 1E; Supplementary
101 Movie 2). The geometry of delaminating cells also changed; at E14.5 cells rounded up for
102 delamination, while at E15.5 cells transitioned instead into axially elongated and basally constricted,
103 wedge-like shapes prior to delamination (Fig. 1D-F).

104 To better understand how these changes in division and delamination strategies relate to cell
105 differentiation, and to identify the mechanisms involved, we turned to fixed tissue imaging. Previous
106 work has implicated the desmosomal cadherin Desmoglein1 (Dsg1) in delamination [15]. At E14.5 no
107 Dsg1 or K10-positive differentiating cells were detected in the basal layer (Fig. 1G). In contrast, at
108 E15.5 Dsg1+ K10+ cells were now observed basally, indicating that these cells had already initiated
109 commitment towards differentiation. These double-positive basal cells exhibited enhanced
110 localization of Dsg1 (Fig. 1H) and E-cadherin (Supplementary Fig. 1C) particularly at apical
111 interfaces, displaying wedge-like shapes similar to delaminating cells seen in live imaging (Fig. 1H).

112 To precisely quantify the shape changes of these K10+-basal cells at E15.5, we performed super-
113 resolution imaging of skin whole mounts. K10+ basal cells were still attached to the basement
114 membrane as shown by α6β4 integrin staining, (Fig. 1I), and displayed a wedge-like shape
115 characterized by decreased basal adhesion length and increased apical adhesion surface (Fig. 1I).
116 Interestingly, integrins were enriched at these narrow basal footprints, indicating that differentiation
117 is initiated prior to complete cell detachment from the basement membrane (Fig. 1J).

118 Collectively, these live imaging experiments are consistent with earlier work on fixed samples
119 showing that at early developmental stages embryos engage both perpendicular cell divisions and
120 rapid delaminations associated with suprabasal divisions to generate suprabasal layers [6-8,10]. Our data
121 further indicates that at E15.5 and E16.5 embryos employ a substantially slower, division-
122 independent delamination process associated with remodeling of cell adhesion and changes in cell
123 shape to position cells suprabasally.

124

A biophysical model predicts that in the presence of a mechanical boundary, delamination depends on the mechanical properties of the delaminating cell

To understand the mechanistic basis for this switch in multilayering strategy, we turned to quantitative mechanical modelling. For this we utilized open-source 3D vertex model code [16] and extended a previously published 3D vertex model of the epidermis [13] (see Supplementary Methods). Similar models were recently used to study clonal dynamics of tumor cells in stratified epithelia [17] and initiation of multilayering in single-layered epithelia [18]. The model consisted of suprabasal cells (brown), basal cells (light blue) and a basement membrane (dark blue; Fig. 2A). A key model feature was basal layer rigidity, governed by cell shape. We therefore parameterized this by Δs, the distance in shape space to the fluid-solid transition [16,19,20] (Fig. 2A, inset). The model also included heterotypic interfacial tensions between basal and adjacent suprabasal cells (σ_a; Fig. 2A, magenta), and a potentially wetting interfacial tension between basal cells and the basement membrane (σ_b ; Fig. 2A green). Previous work [13] had shown that these three "tissue background" parameters (σ_a, σ_b, and Δs) generate a robust mechanical model that is capable of capturing key features of the multilayered tissue architecture observed *in vivo.* A central feature of this mechanical model is generation of a mechanical boundary between the basal and suprabasal layer that ensures that small active mechanical fluctuations do not induce mixing between basal and suprabasal cells, and the layers are robustly separated, as observed at E15.5 onwards.

We first sought to predict whether the presence of a mechanical boundary could explain the embryonic stage-specific differences in delamination speed and shape of the delaminating cell (see Fig, 1), similar to what has been theoretically predicted for cell extrusion in simple epithelia [21]. To this end we specifically altered interfacial tensions of the delaminating cell – lateral σ_{dl}, basal σ_{db}, and apical σ_{da} (Fig. 2B). Past experimental observations [9,22] suggested that basal layer rigidity Δs is also relevant for delamination. We therefore also allowed it to vary while keeping the other "tissue background" parameters σ_b and σ_a fixed. We found that for a cell to move upward into the suprabasal layer in the presence of small active fluctuations, it indeed needed only to change its interfacial tensions (Fig. 2C). We proceeded to precisely predict how changes in delaminating cell mechanics and the mechanical boundary itself alter delamination rates. To quantify these rates, we simulated a large ensemble of conditions (N>85) for each set of model parameters (3240 sets), and measured the fraction of cells that had delaminated in a fixed time window (Δt = 2000 simulation time units, estimated to be 20 – 200 min [23,24], see Supplemental Methods). We found that delamination rates are a complex function of the four variables (σ_{da}, σ_{dl}, σ_{db}, Δs; Supplementary Fig. 2A). To parse the resulting large parameter space, we searched for a data collapse in

158 delamination rates [25], and further investigated whether the rates were consistent with an Arrhenius
159 process governed by an energy barrier, i.e. where the rate is proportional to $e^{-E/kT_{eff}}$, where $k\,T_{eff}$
160 sets the magnitude of active fluctuations [26-28]. We identified a specific combination of model
161 parameters where all delamination rate curves collapsed on top of each other (Fig. 2D; non-collapsed
162 data in Supplementary Fig. 2), indicating that a delaminating cell experiences a mechanical energy
163 barrier to move upwards. Further, this barrier can be modulated by the mechanical properties of the
164 delaminating cell, in the following form:

165 $$E = F(\sigma_{da} - \sigma_{db} + c\,\Delta s)$$

166 Here F is a monotonically increasing function of its argument (see Supplemental Methods). The first
167 two terms indicate that the energy barrier depends on the difference between the basal and apical
168 interface tensions of the delaminating cell. To decrease the energy barrier and delaminate more
169 efficiently, a delaminating cell needs to increase the tension (i.e. decrease the wetting) with the
170 basement membrane, while also decreasing its apical interfacial tension with the suprabasal cells.
171 This is consistent with the experimentally observed emergence of a wedge-like cell shape and apical
172 Dsg1 enrichment from E15.5 onwards (see Fig. 1G-I). The third term indicated that the energy
173 barrier increases with increasing surrounding basal layer rigidity Δs. Interestingly, altering the
174 interfacial tension σ_{dl} of the delaminating cell did not change the delamination rate (Fig. 2D).
175 Overall, these results indicated that the non-mixing of basal and suprabasal cells observed
176 experimentally at E15.5 and E16.5 (see Fig. 1) could be explained by a mechanical boundary
177 between these cell layers, and that cells would be able to cross this barrier by changing their own
178 mechanical properties.

179

180 **A mechanical boundary emerges at E15.5 impacting delamination.**

181 Next, we investigated whether such a mechanical intratissue boundary emerges during development.
182 To this end we performed detailed quantitative morphometry of basal cells across developmental
183 stages. 3D segmentation revealed substantial transformations of cell shapes: whereas basal cells at
184 E14.5 showed considerable shape heterogeneity and a high degree of shape deformation, at E15.5
185 cells shortened and became more cuboidal, and finally transitioned into homogenous, prolate cell
186 shapes at E16.5 (Fig. 3A-C). To infer changes in interfacial tensions from these morphological
187 transitions, we built on previous work suggesting that an apical curvature angle γ and cell height h
188 reflect a force balance along each interface [29,30]. Further, interfacial properties – orientation angle of
189 the lateral interface (β) and the roughness of the apical interface (R) - depend on heterotypic

interfacial tensions [31,32]. We therefore measured these observables *in vivo* in the basal layer (Fig. 3D-H). These measurements revealed a decrease in cell height between E15.5 and E16.5, and non-monotonic behaviors for the lateral interface orientation angle from E14.5 to E16.5 (Fig. 3E), consistent with the observed stage-specific cell shape transitions (Fig 3A-C). As in previous work, R quantifies the tissue-scale roughness – variations between the heights of the lateral junctions across the basal layer (Fig. 3F) – which are distinct from the cell-scale curvatures defined by γ (Fig. 3G). This can be seen by linking the images in Fig 3G to the data in Fig 3E and H - at E15.5 the cell-scale curvature γ is high but over larger length scales the apical surface is relatively flat (low R), while at E14.5 the cell-scale curvature γ is low but with a higher tissue-scale roughness R. At E16.5, γ is even higher than at E15.5, while R is lower that E15.5. Collectively these shape changes were indicative of dynamic, stage-specific changes in apical heterotypic interfacial tension, wetting at the basement membrane, and overall tissue stiffness.

We then proceeded to integrate the experimental quantifications with the 3D vertex model by converting experimental measurements to simulation units, followed by model simulations across a wide range of parameter conditions (Fig. 3D, I, J). For three observables (R, β, h), we discovered that the data could be collapsed as a simple function of the model parameters (Fig. 3I; Supplementary Fig. 3.A-C). As a result, the average value of each *in vivo* observable (Fig. 3E, H) specified a point on the y-axis of the respective simulation plot (Fig. 3I), and therefore generated a unique constraint on the model parameters. Although the curved interfaces described by γ are not explicitly embedded in 3D vertex models, we can use the assumption of force balance[29,30] to write γ directly as function of σ_b and Δs (Fig. 3J), and thereby directly extract a fourth constraint on vertex model parameters. Collectively this benchmarking process of *in vivo* measurements to simulations resulted in a set of four constraint equations for the three unknowns (σ_b, σ_a, Δs) at each developmental stage (Fig. 3D); we solved this system of equations for the best-fit model parameters at each stage using a standard over-constrained solver[33] (Fig. 3K; see Supplementary Methods).

These data demonstrated that at E14.5, the basal layer is nearly fluid-like, with very low tissue stiffness parameterized by Δs (Fig. 3N). At this stage the interfacial tension between basal and suprabasal cells is low, coupled to a positive interfacial tension at the cell-basement membrane interface, suggesting only low levels of integrin-based wetting. At E15.5, the tension at the basement membrane interface became nearly zero, suggesting wetting behavior (Fig. 3K). This was accompanied by increased interfacial tension at the basal-suprabasal interface, as well as increased basal layer stiffness (Fig. 3K). At E16.5, similar trends remained, while tissue stiffness increased further (Fig. 3K). Combined, these changes generated a four-fold increase in the magnitude of the

223 mechanical energy barrier for a basal cell to delaminate from E14.5 to E15.5 (Supplementary Fig.
224 3F-H).

225 Building on our understanding from the data collapse in Fig. 2, we were then able to collapse the
226 rates of delamination as a function of the differences in the interfacial tensions between the
227 delaminating cell and the background basal cells at the apical ($\Delta\sigma_{da,a}$) and basal ($\Delta\sigma_{db,b}$) interfaces
228 (Fig. 3L; Supplementary Methods Fig. 3C, see Supplemental Methods). This analysis showed that at
229 E14.5, the probability of a standard basal cell (0.0 on the x-axis of Fig 3L) delaminating during the
230 time window Δt was less than 20%, but only a small change in basal and apical tensions (~15%, 0.15
231 on the x-axis in Fig 3L) was sufficient to generate a massive increase in delamination probability,
232 increasing it to nearly 100% in the same time window. In contrast, at E15.5 and E16.5, a basal cell
233 must change its mechanical properties substantially (by appr. 40%, 0.4 on the x-axis of Fig. 3L) in
234 order to generate a similar increase in delamination probability.

235 Collectively, these data suggest that a mechanical boundary forms between the basal and suprabasal
236 layers at around E15.5, thus requiring cells to have a robust mechanism to commit to delamination
237 and overcome this barrier, while such a mechanism is not necessary at E14.5.

238

239 **A committed basal population characterized by Notch activation emerges at E15.5**

240 To identify the molecular driver for this predicted mechanical state change required for delamination
241 at E15.5 and later, we investigated the evolution of epidermal cell states using single cell RNA
242 sequencing (scRNAseq; Fig. 4A). We obtained single-cell suspensions of skin from E13.5, E14.5,
243 E15.5. and E16.5 embryos, isolated and sequenced in parallel to avoid batch effects (Fig. 4A). The
244 quality-controlled and filtered dataset, obtained from 2 biological replicates/stage, comprised of
245 >15,000 cells/stage that were annotated based on known marker genes (Supplementary Fig. 4A, B).
246 Focusing on the epidermal (non-hair follicle) clusters, we identified cycling and non-cycling basal
247 cells as well as suprabasal cell states (Supplementary Fig. 4C, D). Leiden clustering revealed that cell
248 states were clustered separately according to their developmental stage, indicating that key cell states
249 (basal and suprabasal cells) underwent substantial transcriptional changes in transcriptomes while
250 progressing through development (Fig. 4B).

251 Closer inspection of key differentiation genes such as *Krt1*, *Krtdap* and *Notch1* revealed that at E14.5
252 their expression was restricted to the suprabasal cell populations. In contrast, at E15.5 and E16.5 a
253 subset of basal cells also showed expression of differentiation genes (Fig. 4C), in agreement with

254 some basal cells showing K10 and Dsg1 expression at this stage (Fig.1G, H) . To conclusively
255 identify a committed basal cell population, we examined a Harmony integrated dataset of E14.5-
256 E16.5 epidermal cells. Leiden clustering of this integrated dataset revealed a distinct population of
257 cells characterized by expression of both basal stem cell (e.g. *Trp63* and *Itga6*) and terminal
258 differentiation genes (Supplementary Fig. 4E, F), indicating that only from E15.5 onward, a subset of
259 basal cells commit to differentiation. Next to this hybrid transcriptional signature of differentiation
260 and stemness, this subset of committed basal cells also showed enhanced expression of the suprabasal
261 adhesion proteins E-cadherin and desmoglein (Fig. 4D), consistent with a downregulation in
262 heterotypic interfacial tension between the committed cell and suprabasal cells predicted by the
263 model (Fig. 2D and 3O).

264 As Notch activity has been shown to be critical for terminal differentiation in keratinocytes [34], we
265 examined Notch pathway activity specifically in the basal layer. Receptor-ligand enrichment analyses
266 (CellPhoneDB; [35] predicted increased basal activity of especially Notch1-Jagged2 signaling from
267 E15.5 onward (Fig. 4E). Indeed, immunofluorescence analysis revealed that Notch activity (cleaved
268 intracellular domain; N-ICD), was detected in single cells only in the basal layer of E15.5 and E16.5
269 epidermis, but not at E14.5 (Fig. 4F, G). Intriguingly, these Notch1-active cells were also positive for
270 the differentiation marker K10 and displayed a wedge-shaped morphology (Fig. 4F), indicating that
271 these cells are committed to differentiation and undergoing delamination as observed by the
272 K10/Dsg-1 positive cells (Fig.1G, H)

273 Collectively these data indicated the emergence of a committed basal cell state characterized by a
274 hybrid profile of stemness and differentiation, a change in cell shape, a switch to a suprabasal cell
275 adhesion profile and Notch activity.

276 **Generation of the mechanical boundary at E15.5 is concomitant with stiffening of the basement**
277 **membrane and rigidification of the basal layer**

278 We hypothesized that maturation of the tissue and specifically the basement membrane could drive
279 the emergence of the mechanical barrier at E15.5. Combined analysis of the scRNAseq data (Fig.
280 5A) and quantitative multiplex tissue imaging using Imaging Mass Cytometry [36], revealed an
281 increase in basement membrane maturation and cell-matrix adhesion (Fig.5A-C; Supplementary Fig.
282 5A). Importantly, collagen IV, a key component of the basement membrane that is essential for its
283 rigidification and stabilization, was increased from E14.5 to E16.5 (Fig. 5B-C), suggesting
284 maturation of the BM from E14.5-16.5. In agreement, the hemidesmosomal α6β4 integrin was also
285 increased during this transition, and became more and more confined to the epidermal-dermal

286 junction (Fig. 5B, C; Supplementary Fig. 5A). Consistently, atomic force microscopy-mediated force
287 spectroscopy confirmed a significant stiffening of the basement membrane from E14.5 to E16.5 (Fig.
288 5D).

289 Based on observations in other systems that link changes in tension to mechanical boundary
290 formation [9,16,19,20,22,37,38] we speculated that this change in tissue mechanics promoted establishment
291 of a mechanical boundary between basal and suprabasal cells. Quantification myosin phosphorylation
292 (pMLC2) indicated increased actomyosin tension at apical cell-cell junctions and specifically at the
293 interface between basal and suprabasal cells at E15.5 compared to E14.5 (Fig. 5E), providing further
294 support for the geometry-based tension inference indicating emergence of a mechanical boundary
295 (Fig. 3N). Furthermore, analyses of cell shapes and tissue dynamics from live imaging showed that
296 the cells in the basal layer of E14.5 embryos were larger and more irregular shaped compared to cells
297 at E15.5, as already seen in fixed tissue imaging (Fig. 5F, G; Fig. 3 A-C; Supplementary Movie 3). In
298 agreement, at E15.5 cell density was increased, (Fig. 5F, H), with decreased mobility of the basal
299 layer cells as quantified by particle image velocimetry (Fig. 5F, I; Supplementary Movie 3), in line
300 with previous *in vitro* work implicating a jamming transition in initiation of delamination [9]. Together,
301 these changes were consistent with a tissue-scale rigidity transition in the developing epidermis that
302 occurs from E14.5-16.5, from an initially floppier basement membrane and a fluid-like basal layer to
303 a stiff basement membrane and a jammed basal layer with enhanced cell-matrix adhesion and apical
304 actomyosin tension.

305

306 **Tissue rigidity and cell shape changes drive Notch-dependent delamination and control of**
307 **tissue crowding**

308 We next investigated whether the changes to tissue rigidity are sufficient to induce basal layer
309 jamming and the emergence of a mechanical barrier. For this we mimicked tissue maturation *in vitro*
310 by modulating cell density and substrate rigidity by engineering micropatterned adhesive islands on
311 polyacrylamide hydrogels of defined stiffness (Fig. 6A). Culturing primary epidermal progenitors on
312 micropatterned islands revealed that increasing substrate stiffness under confinement not only
313 substantially enhanced differentiation (Fig. 6B), but, importantly, promoted efficient suprabasal
314 separation of these differentiated cell populations from the undifferentiated cells that remained
315 basally positioned (Fig. 6C), indicating that increasing substrate stiffness is sufficient to induce
316 boundary formation.

317 As the emergence of basal committed cells was associated with Notch activity (Fig. 4D), we then
318 asked whether basal layer crowding was sufficient to induce Notch signaling. For this, we performed
319 live imaging of primary epidermal progenitors isolated from Notch1 activity reporter mice [39] to
320 identify whether and when Notch signaling is activated in basal cells triggered to differentiate and
321 form a suprabasal layer (Fig. 6D). As expected, all progenitors were initially Notch-reporter negative,
322 but upon application of calcium to trigger differentiation and multilayering, individual cells gradually
323 switched on the reporter followed by delamination (Fig. 6D; Supplementary Movie 4). Intriguingly,
324 prior to turning on Notch1 signaling these cells were more elongated and resided in denser tissue
325 regions than reporter negative-cells (Fig. 6D), thus indicating that crowding and increased cell-cell to
326 cell-matrix contact area promoted Notch activation.

327 We then asked whether Notch1 transcriptional activity is necessary for cell fate commitment and
328 delamination by deleting the Notch transcription factor, Rbpj, in the epidermis (Rbpj-KO; [40,41]). At
329 E14.5, the epidermis of Rbpj-KO mice appeared largely comparable to control littermates (Fig. 6E).
330 At E15.5, and more prominently at E16.5, the epidermis became structurally more abnormal,
331 characterized by a specific thinning of the suprabasal differentiated layers (Fig. 6F). Moreover, basal
332 cells were increased in height and became more columnar in E15.5 and E16.5 Rbpj-KO mice
333 compared to controls (Fig. 6G), accompanied by higher cell density (Fig. 6D), indicating increased
334 crowding of the basal layer. To examine if this increased crowding was due to reduced commitment
335 to differentiation or decreased delamination, we quantified differentiating, delaminating cells. We
336 observed emergence of the committed basal cell population in both control and Rbpj-KO epidermis
337 (Fig. 6H), indicating that the initial commitment to differentiate does not depend on Notch
338 transcriptional activity. Instead, we observed an increase in the number of wedge-shaped committed
339 cells undergoing delamination at this stage (Fig. 6H), suggesting an inability to overcome the
340 mechanical energy barrier and move suprabasally.

341 To identify the molecular mechanism by which Notch transcriptional activity regulates efficient
342 delamination, we performed scRNAseq analysis across E14.5-E16.5 from control and Rbpj-KO
343 mouse skin. Overall, basal cell populations were transcriptionally similar between controls and Rbpj-
344 KO mice (Fig. 6I). However, as described previously [34], Rbpj-KO cells of all developmental stages
345 displayed impaired terminal differentiation (Fig. 6I; Supplementary Fig. 6A). Intriguingly, at E15.5 a
346 distinct Leiden cluster representing committed basal cell population emerged, mainly composed of
347 Rbpj-KO cells (Fig. 6I, J; Supplementary Fig. 6B). Consistently, at E16.5 the Leiden cluster
348 consisting of committed cells was dominated by Rbpj-KO cells (Fig. 6I, J; Supplementary Fig. 6B),

349 validating the immunofluorescence observations that Rbpj-KO still commit to initial differentiation
350 but cannot efficiently delaminate, leading to accumulation of committed basal cells.

351 To identify master transcriptional switches downstream of Notch that drive the final step of
352 delamination, we performed differential gene expression analyses of committed cells between control
353 and Rbpj-KO at E15.5 and E16.5. This analysis identified two interesting significantly altered
354 regulators in Rbpj-KO committed cells: the zinc finger protein Zpf800, a master regulator of
355 intestinal stem cell differentiation [42], was not upregulated (Fig. 6K left panel; Supplementary Fig. 6C,
356 D). At the same time Rbpj-KO basal cells failed to downregulate the Ep300 Inhibitor of
357 Differentiation (Eid1) (Fig. 6K, right panel). Eid1 acts as a transcriptional repressor through
358 inhibition of p300-mediated H3K27 acetylation (H3K27ac), thus preventing the activation of
359 enhancers that promote differentiation [43,44]. Indeed, RNA *in situ* hybridization and quantitative
360 immunofluorescence confirmed that while control embryos downregulated Eid1 in the suprabasal
361 layers and, as a consequence, showed substantially reduced H3K27ac levels in delaminating cells and
362 suprabasally, Rbpj-KO embryos maintained both high Eid1 and H3K27ac in delaminating cells and
363 suprabasal layers, in line with reduced differentiation (Fig. 6L).

364 Collectively, these data demonstrate that stiffening of the substrate is sufficient to drive basal layer
365 jamming and the formation of a mechanical barrier between basal and suprabasal compartments. This
366 basal layer jamming and crowding then triggers Notch signaling required for completion of
367 delamination and control of basal layer density.

368

369 **Discussion**

370 Here we show that the developing epidermis employs different strategies for multilayering that are
371 driven by changes in tissue mechanics. Early during development of this stratified epithelium, there
372 is no substantial mechanical energy barrier between basal and suprabasal cell layers. This allows fast
373 upward movement of basal cells independent of basal fate commitment by either dividing
374 perpendicularly or detaching quickly in order to rapidly establish a stratified tissue. Similar
375 mechanical-instability-driven mechanisms have been proposed by previous modeling [18,21]. At later
376 stages (E15.5 and beyond), maturation and stiffening of the basement membrane enhance basal cell-
377 matrix adhesion and crowding to rigidify the tissue, generating a substantial mechanical boundary
378 between basal and suprabasal cells. In order to cross this boundary, cells from this stage on must now
379 commit to differentiation and undergo subsequent transcriptional rewiring, controlled by Notch
380 activation, to complete delamination. Interestingly, this delamination process in the matured
381 epidermis is substantially slower than the rapid detachment observed by us and others in early

embryonic development[9,10]. As Notch activation itself is regulated by tissue rigidification and crowding, as also found in other systems[45,46], it suggests an elegant control mechanism for homeostasis in an open niche not characterised by clear geometrical cues: tissue crowding itself is sufficient in a rigidified tissue to trigger Notch activation necessary to control the rate and timing of delamination. This feedback loop thus allows accurate control over the densities of both basal and suprabasal layers in coordination with compartmentalization of stem cells and differentiated progeny. Many open questions remain. A key open question is how the system decides which subset of cells in the basal layer becomes committed and Notch active. Previous work has suggested that since Notch is a surface receptor, its activity depends on tissue crowding together with associated cell shape and surface area changes that regulate the density of such receptors [46-48]. This could explain the emergence of Notch active cells in elongated cells within dense regions – these cells would have transiently maximized surface area to receive Notch ligand signal from their neighbors. Previous work has investigated a 2D vertex model where cell fate decisions are coupled to cell areas [49], which may be a useful starting point for predicting features we observe here. Future modeling work should focus on understanding how changes to tissue stiffness and cell shape induce Notch signaling in a 'correct' subset of basal cells (e.g. they are spaced out and the right fraction depending on the degree of crowding), and on adding the effects of differently oriented cell divisions in basal layer — in different developmental stages – to the 3D model.

Downstream of Notch signaling, it will be intriguing to understand how the transcriptional reprogramming, involving Eid1and Zfp800 associated with global changes in H3K27ac translates to control of delamination timing. It is interesting to note that the direct downstream targets of Eid1- the histone acetyltransferases P300 and CBP - are evolutionarily conserved maintenance factors of lineage-specifying core-transcriptional networks. They function as transcriptional rheostats that control global H3K27ac levels, where the duration of their activity determines the long-term impact on chromatin state [50,51]. Upon their inhibition, >8h of hypoacetylation is required to trigger a permanent switch and "point of no return" to H3K27me3-mediated chromatin silencing [50]. Intriguingly, this is the approximate duration of the slower delamination process after E15.5. Thus, Notch may function as a mechanical sensor to ensure that terminal differentiation is not initiated prematurely in areas of low basal cell density. Precise coordination of onset of terminal differentiation with basal stem cell layer density is likely to be a critical feature in dynamically self-renewing tissues with an "open stem cell niche". Collectively, we propose that in such tissues mechanical boundaries are required to separate biological activities of cycling stem cells and post-mitotic terminally differentiated cells. Here, precisely controlled cell state transitions control the transit between the compartments to robustly maintain tissue homeostasis and barrier integrity.

416

417 **Methods**

418 **Mice**

419 Membrane-targeted Tomato reporter mice (R26R$^{mT/mG}$), nucleus-targeted Tomato reporter mice
420 (R26R$^{nT/nG}$) and high-activity Notch1 activation-dependent reporter mice (N1IP: CreHI) were from
421 were from JAX laboratories (stock #007676, #:023035 and #027234 respectively). Rbpj floxed mice
422 were obtained from JAX (stock # 034200) and crossed with the K14-Cre line [40] to obtain epidermis-
423 specific depletion. Embryos were staged based on vaginal plug (taken as embryonic day 0) and limb
424 morphology. All mouse studies were approved and carried out in accordance with the guidelines of
425 the Ministry for Environment, Agriculture, Conservation and Consumer Protection of the State of
426 North Rhine-Westphalia (LANUW; 81-02.04.2022.A065; and 2024-155), Germany.

427

428 **Ex vivo embryo imaging**

429 Imaging was performed essentially as described earlier [9,13]. Briefly, embryos were dissected at
430 embryonic stages E14.5 or E15.5 and immobilized on custom-built imaging chambers engineered on
431 top of Lumox-teflon imaging plates to allow gas exchange (Sarstedt). Whole embryos were
432 immersed in epidermal growth medium (CnT-PR, CELLnTEC Advanced Cell Systems)
433 supplemented with calcium-depleted 10% fetal bovine serum (HyClone/Thermo Fisher), 20 U/ml
434 penicillin-streptomycin (Thermo Fisher), 20 mM Hepes, 1.8 mM CaCl2, and 10 ng/ml mouse
435 recombinant EGF (Novus; NBP2-34952). Imaging was performed using an Andor Dragonfly 505
436 high-speed spinning disk confocal microscope (Oxford Instruments) with an inverted Nikon Eclipse
437 Ti2 microscope (Nikon) equipped with 488 nm and 546 nm lasers, an Andor Zyla 4.2 sCMOS
438 camera and an environmental chamber set at 37°C, 5% CO2 using a 40X dry objective. Images were
439 acquired using Fusion 2.0 software (Andor). After acquisition, the image series were 3D drift
440 corrected using the ImageJ plug-in Fast4Dreg [52] combined with manual registration, if required.

441

442 **Immunofluorescence and confocal microscopy**

443 For skin whole mounts, embryos were dissected from pregnant mice and directly fixed in pre-
444 warmed (37°C) 4% paraformaldehyde (PFA) at room temperature for 3 h. After multiple PBS
445 washes, the skin was carefully peeled using forceps and placed in blocking solution (0.5% Triton-X,
446 5% bovine serum albumin (BSA), 3% normal goat serum (NGS)) for 1 h at room temperature. For
447 paraffin sections tissue biopsies were fixed in 4% PFA, embedded in paraffin and sectioned. Sections
448 were de-paraffinized using a graded alcohol series and antigen retrieval was carried out using target

449 retrieval solution (Dako) at pH 6 or pH 9 in a pressure cooker. For cryosections, tissue samples were
450 placed unfixed into cryomolds, embedded in OCT (Tissue Tek) and allowed to harden on dry ice. 8
451 μm thick sections were cut, air-dried and fixed with 4% PFA. For both paraffin and cryofixed
452 sections, samples were blocked in 5% BSA, 3% NGS. For paraffin sections antibodies were diluted
453 in Dako antibody diluent (Agilent). For cryosections antibodies were diluted in blocking solution.
454 Cultured epidermal cells were fixed in 4% PFA for 15 min at room temperature After PBS washes,
455 samples were placed in 0.3% Triton-X, 5% BSA for one hour at room temperature after which
456 primary antibodies were diluted in the same solution. In all cases antibodies were incubated overnight
457 in moist chamber at 4°C. Following PBS washes, secondary antibodies were diluted in 1% BSA in
458 PBS and incubated for 1h at room temperature.
459
460 For super-resolution imaging of Actin (Phalloidin), K10, Dsg1, E-cadherin, and Integrin α6, the
461 embryos were fixed in pre-warmed 4% PFA at 37°C for 1 hour and rinsed with PBS. The back skin
462 was peeled using forceps and incubated in blocking solution (2% Triton-x, 5% BSA in PBS) for 24
463 hours at 37°C. Primary antibodies were diluted in the blocking solution and incubated 48 hours at
464 37°C on shaker followed by several washes with 2% Triton-X with a final overnight wash.
465 Secondary antibodies were diluted in blocking solution and incubated 24 hours at 4°C followed by
466 several washes with 2% Triton-X.
467 For pMLC2 staining embryos were fixed in 4% PFA dissolved in HBSS for 1 hour on a shaker at
468 room temperature. Back skins samples are then peeled and permeabilized with 0.02% PBS-Tween 20
469 for 30mins and blocked with blocking solution (5% NGS,1% BSA) for 2 hours before incubating
470 with primary antibody overnight in 4ºC. Samples are then thoroughly washed with 0.02% PBS-
471 Tween 20, incubated with secondary antibodies at 1:400 dilution for 1 hour at room temperature and
472 washed. All tissue samples were mounted in Elvanol.
473 The following primary antibodies were used: guinea-pig anti-Keratin 10 (Progen, #GP-10; 1/300);
474 rabbit anti-p-MLC2 (p-Ser19; Cell Signaling, 3675; 1:200), rabbit anti-cleaved-Notch1 (Cell
475 signaling; #4147S; 1/50), mouse anti-Desmoglein 1/2 (Progen, #61002; 1/200), rabbit anti-TGM1
476 (360; Proteintech, #12912-3-AP; 1/300), rabbit anti P63 (Genetex #GTX102425; 1/100), guinea-pig
477 anti-Keratin 14 (Progen, GP-CK14; 1:300), mouse anti E-cadherin (BD Biosciences, #610181;
478 1/200), rabbit anti Cyclin B1 (Cell Signaling, #4138S; 1/200), mouse anti H3K27ac (Active Motif,
479 #39685, 1/200), rat anti integrin α6 (Biorad #MCA699; 1/200) . F-actin was detected using Alexa-
480 Fluor-conjugated phalloidin (1:500). Bound primary antibody was detected by incubation with
481 Alexa-Fluor 488-, 568- or 647 -conjugated antibodies (Invitrogen). Nuclei were counterstained with

482 4′, 6-diamidino-2-phenylindole (DAPI, Invitrogen). Slides were mounted in Elvanol.
483 Fluorescence images were collected by laser scanning confocal microscopy (LSM980; Zeiss) with
484 with Zeiss ZEN Microscopy software (Zeiss ZEN version 3.7) using a 40X water immersion
485 objective. Images were acquired at room temperature using sequential scanning of frames of 1 µm
486 thick confocal planes (pinhole 1). Images were collected with the same settings for all samples within
487 an experiment. For super-resolution imaging a 63X oil objective and the Airyscan 2 SR (super-
488 resolution) mode with default resolution settings were used. Laser power and image size were kept at
489 a minimum to avoid photo-bleaching. All airyscan images were 3D processed using the Zeiss
490 Airyscan Processing mode with auto filter and standard strength.
491
492 **Embryonic epidermal vertex analysis**
493 Membrane-tomato positive E14.5, E15.5 and E16.5 embryos were isolated, fixed immediately in
494 4%PFA over night at 4°C and washed in PBS. The back skin was then removed using micro-scissors
495 and forceps and permeabilized in PBS/0.5% Triton-X for 1h at RT. Nuclei were stained by
496 incubating the skin in DAPI diluted in DAKO antibody diluent for 1h at RT. The skin was then
497 mounted in Mowiol.
498
499 Confocal stacks were recorded at a voxel size of X: 0.361, Y: 0361, Z:0.299 using a Leica SP8
500 equipped with an APO CS2 63x/1.40 oil objective. To determine basal cell vertices, confocal stacks
501 were processed in Imaris and minimal XZ or YZ projection were exported using the extended section
502 view. Using the segmented line tool in ImageJ a line was drawn across the apical and basal vertices
503 of basal cells. Coordinates were extracted and "Julia" was used in Visual Code Studio to determine
504 cell height (h), apical and basal vertex distances (a) and the lateral interface orientation (angle beta).
505 The lines connecting the basal and apical vertices, respectively, were used to determine the apical
506 layer roughness (R) (See also Supplementary Methods). The apical curvature angle gamma was
507 determined manually using the angle tool in ImageJ.
508
509 **Image analyses**
510 For tissue-scale analysis, 2D segmentation were performed from live imaging data on
511 whole embryos or cultured epidermal progenitor monolayers using Cellpose4SAM (v4.0.8) [53]. 2D
512 cell shape parameters were measured using custom Python script and cell densities were measured
513 using ImageJ. For 3D analyses of cell shapes of delaminating cells from embryo live imaging, Imaris
514 11 was used to manually create 3D surfaces of delaminating and corresponding neighboring basal
515 cells. For 3D segmentation of basal cells from super resolution images, K10 negative basal cells were

manually segmented in 3D using Imaris. Meshes were exported from Imaris surfaces after which shapes were analyzed by quantifying Spherical Harmonics [54] using a custom Python script.
In fixed tissue samples, basal committed cells and delaminations were identified based on the expression of specific markers (K10 and/or Desmoglein) and their contact with the basement membrane, and subsequently manually counted. Active-Notch positive cells were quantified manually. The method was applied across all stages and conditions. Integrin α6, E-cadherin and Desmoglein mean intensities were manually measured at the basal, apical and lateral membranes on Image J. To quantify epidermis thickness, the distance between epidermal basement membrane and most superficial point of the epidermis was measured. To quantify specifically the basal layer thickness versus the differentiated layer thickness, the expression of specific markers (K10 and desmoglein) has been used to distinguish the differentiated layers (K10+) from the basal layer.
To measure boundary straightness between the bottom and upper layers in micropatterns of soft and stiff polyacrylamide (PAA) hydrogels, both a segmented line following the top of each nucleus in the bottom layer and a straight line were drawn. The lengths of these lines were measured using ImageJ, and the ratio of the straight line to the segmented line was calculated.
Eid1 RNA signal was quantified by segmenting suprabasal cells based on Keratin-DAP–positive cells. Mean fluorescence intensity of Eid1 mRNA was measured using Fiji.

3D vertex model

A dynamic three-dimensional model of stratified epithelial tissues was developed using the 3D vertex framework (Zhang and Schwarz, 2022). In the 3D vertex model, cells are represented as polyhedra, each characterized by a homeostatic volume V_0 and surface area S_0. The geometry of each cell is defined by its vertices, which serve as the degrees of freedom of the system. The modeled epithelium consists of two main cell compartments. The upper compartment represents the suprabasal differentiated cell layer, while the middle one-cell-thick layer corresponds to the basal stem cell layer. Because the vertex model treats cells as space-filling polyhedra, we modeled the basement membrane as an additional layer of interconnected "cellular network" directly attached beneath the basal layer. In this framework, cells exert forces on one another through shape-based interactions governed by the following energy functional :

$$E = \sum_{\alpha} K_S (S_\alpha - S_0)^2 + \sum_{\alpha} K_V (V_\alpha - V_0)^2 + \sum_{\alpha\beta} \boldsymbol{\sigma}_{\alpha\beta} S_\alpha \quad (1)$$

The first term of the energy functional describes the competition between contractile forces generated by cell actomyosin networks (which enable cells to minimize their shape or surface area to resist their environments), and adhesive forces mediated by cadherin-based, which promote the elongation of cell–cell contacts during neighbors' exchange (T1s). The second term accounts for the mechanical resistance of cells to volume fluctuations, as most cells are fluid-filled and resist changes in volume. The third term incorporates heterotypic interfacial tension σ_a between the basal cells and suprabasal cells, and the tension σ_b associated with integrin-based wetting behaviors at basal-basement membrane interface.

Previous studies have shown that differential expression of adhesion molecules and cytoskeletal components associated with cell fate specification (through variations in protein or gene expression) can modify cell–cell interactions, leading to differences in adhesion strength and heterotypic interfacial tension [9,13,55-63]. Such tension differences are known to play a central role in establishing and maintaining sharp tissue boundaries [61]. Moreover, basal cells adhere to the basement membrane via integrins, which introduce a wetting interaction characterized by σ_b [64]. The parameters K_S and K_V denote the elastic moduli associated with the surface area and volume of the cells, respectively. Upon non-dimensionalization, this energy functional allows the definition of a key order parameter known as the target shape index, $s_0 = S_0 V_0^{-\frac{2}{3}}$, which controls the mechanical rigidity of the tissue. By tuning s_0, the epithelial confluent tissue exhibits a rigidity transition from a solid-like to a fluid-like state, with a critical value at $s_0 = 5.4$ [16,20].

To quantitatively predict the mechanical parameters and cellular mechanisms underlying mechanical barrier formation between the basal and suprabasal layers, we first simulated the epithelium in the absence of cell delamination. The system evolves according to overdamped Langevin dynamics, where vertex positions are continuously updated to minimize the total mechanical energy:

$$\partial_t r_i = -\mu \nabla_i E_i + \sqrt{2D_t}\, \boldsymbol{\eta}(t). \qquad (2)$$

The left-hand side represents viscous drag forces, the first term on the right-hand side corresponds to interaction forces derived from the energy potential, and the second term represents thermal fluctuations in vertex positions r_i . Here $\boldsymbol{\eta}$ is an uncorrelated stochastic Gaussian white noise with unit amplitude, $D_t = \mu k_B T_{\text{eff}}$, where μ is the mobility (inverse frictional drag), k_B Boltzmann constant, and T_{eff} is an effective temperature parameter that sets the scale of the fluctuations. Unless otherwise noted, for our simulations we choose $\mu = 1,\ k_B = 1$ and $T_{\text{eff}} = 0.002$. This choice of T_{eff}

580 allows fluctuations of interface lengths but is not sufficient to generate diffusion or fluidity in the
581 basal layer.

582 From the simulated model, we can compute the effective tensions governing different interfaces: a)
583 The homotypic tension between basal cells $\sigma_{bb} = 4K_S\Delta s_b$ where $\Delta s = s_\alpha - s_0$ measures the basal
584 layer stiffness (and $\Delta s = 0$ at the transition point); b) The effective heterotypic tension at the basal-
585 suprabasal interface $\Gamma_a = 2\sigma_a + 2K_s(\Delta s_s + \Delta s_b)$, where Δs_s the stiffness of the suprabasal layer; c)
586 The effective wetting tension $\Gamma_{bm} = 2\,\sigma_b + 2K_s(\Delta s_b + \Delta s_m)$ between basal cells and the basement
587 membrane (constituted of a cellular network with a small shape parameter). Unless otherwise
588 noted, $\Delta s_m = 0.26$, which ensures the basement membrane remains very stiff and solid-like.
589
590 For more detailed description see Supplementary Methods.
591
592 **Single-cell RNA sequencing (scRNAseq)**
593 E13.5, E14.5, E15.5 and E16.5 embryos from wild type, control or K14Cre-RBP-J floxed/floxed
594 mice (two embryos/genotype/stages) were collected simultaneously and back skins were peeled off.
595 Single-cell suspensions were generated by enzymatic digestion by incubating back skin tissues in a
596 mixture of DNAse I (40 µg/ml), Liberase (0.125 mg/ml; Roche Cat. NO. 05401119001), and papain
597 (30 U/ml; Worthington) in Minimum Essential Medium, Spinner modification (Gibco 11380) for 15
598 min (E13.5), 20 min (E14.5), 30 min (E15.5) or 40min (E16.5) at 37°C followed by mechanical
599 dissociation. The reaction was stopped with 22% FBS and single cells were washed with FACS
600 buffer (0.2% chelated FBS, 2 mM EDTA in 1x DPBS (Sigma Aldrich, D8537)). For wild type
601 sequencing, cells were labeled with BD Mouse Single-Cell Multiplexing Kit (Cat # 633793): E13.5
602 rep 1: Sample Tag (ST) 1; E13.5 rep 2: ST 2; E14.5 rep1: ST 3; E14.5 rep2: ST 4; E15.5 rep1: ST 5;
603 E15.5 rep2: ST 6; E16.5 rep1: ST 7, E16.5 rep2: ST 8. For K14Cre-Rbpj floxed and control
604 sequencing, surface biotinylation was used [65]. Briefly, cells were labeled with 50 µg/mL EZ-Link
605 sulfo-NHS-biotin (Thermo Fisher Scientific, 21217) on ice for 10 min, followed by incubation in
606 0.6 µg/ml TotalSeq-A PE streptavidin hashtag antibodies (BioLegend) for 30 min on ice as follows:
607 E14.5 Rbpj-KO 1: TotalSeq-A0951 PE Streptavidin 405251 ; E14.5 Rbpj-KO 2: TotalSeq™-A0952
608 PE Streptavidin 405253; E14.5 control 1: TotalSeq-A0953 PE Streptavidin 405255; E14.5 control 2:
609 TotalSeq-A0954 PE Streptavidin 405257; E15.5 Rbpj-KO 1: TotalSeq-A0951 PE Streptavidin
610 405251 ; E15.5 control 1: TotalSeq-A0953 PE Streptavidin 405255; E15.5 control 2: TotalSeq-
611 A0954 PE Streptavidin 405257; E16.5 Rbpj-KO 1: TotalSeq™-A0951 PE Streptavidin 405251 ;
612 E16.5 Rbpj-KO 2: TotalSeq-A0952 PE Streptavidin 405253; E16.5 control 1: TotalSeq-A0953 PE

613 Streptavidin 405255; E16.5 control 2: TotalSeq-A0954 PE Streptavidin 405257. Labeled cells were
614 loaded on a microwell cartridge of the BD Rhapsody Express system (BD) following the
615 manufacturer's instructions. Single-cell whole transcriptome analysis libraries were prepared
616 according to the manufacturer's instructions using BD Rhapsody WTA Reagent kit (633802; BD),
617 except for the Rbpj-KO and control sample tag libraries in which totalseq-ADT-oligo1 (5'-
618 TGCTCTTCCGATCTTGGCACCCGAGAATTCCA-3') primer in place of Sample Tag PCR1 and
619 Sample Tag PCR2 primers during the Sample Tag library amplification [65]. Libraries were sequenced
620 on the Illumina NextSeq 500 using High Output Kit v2.5 (150 cycles; Illumina) for 2 × 75-bp paired-
621 end reads with 8-bp single index aiming sequencing depth of >20,000 reads per cell for each sample.
622
623 **scRNAseq analyses**
624
625 *Read Data QC and Mapping*
626 Illumina sequencing results were demultiplexed and converted to FASTQ format using Illumina's
627 bcl2fastq software (version 2.20.0.422). For K14Cre-RBP-J floxed/floxed data a custom
628 demultiplexing script was used to assign barcodes to sample tags (rhapsody-demultiplex with
629 parameters '-w BD_CLS1_v2.txt BD_CLS2_v2.txt BD_CLS3_v2.txt -a
630 TGGCACCCGAGAATTCCA <fastq files> sample_tags.txt', and sample tags as described above).
631
632 Preprocessed read data was aligned to the mouse reference genome (GRCm39) and counted with
633 STAR [66] (version 2.7.11b) through its single-cell functionality STARsolo, using the following
634 parameters:
635
636 WT: `--runThreadN 16 --soloType CB_UMI_Complex --soloCellFilter None --outSAMtype BAM
637 SortedByCoordinate --soloFeatures Gene GeneFull GeneFull_Ex50pAS --soloAdapterSequence
638 NNNNNNNNNGTGANNNNNNNNNGACA --soloCBmatchWLtype 1MM --soloCBposition
639 2_0_2_8 2_13_2_21 3_1_3_9 --soloUMIposition 3_10_3_17 --soloCBwhitelist BD_CLS1_v2.txt
640 BD_CLS2_v2.txt BD_CLS3_v2.txt --runRNGseed 1 --soloMultiMappers EM --readFilesCommand
641 zcat --outSAMattributes NH HI AS nM NM MD jM jI MC ch CB UB GX GN`
642
643 K14Cre-RBP-J floxed/floxed: `--soloType CB_UMI_Complex --soloAdapterSequence
644 NNNNNNNNNGTGANNNNNNNNNGACA --soloCBposition 2_0_2_8 2_13_2_21 3_1_3_9 --
645 soloUMIposition 3_10_3_17 --soloBarcodeReadLength 0 --soloCellFilter None --soloCBwhitelist
646 BD_CLS1_v2.txt BD_CLS2_v2.txt BD_CLS3_v2.txt --soloCBmatchWLtype 1MM --

soloUMIfiltering MultiGeneUMI_CR --soloUMIdedup 1MM_CR --outSAMtype BAM SortedByCoordinate --soloFeatures Gene GeneFull GeneFull_Ex50pAS --soloMultiMappers EM --outSAMattributes NH HI AS nM NM MD jM jI MC ch CB UB GX GN --outSAMmultNmax 1 --outMultimapperOrder Random --runRNGseed 1 --outFilterScoreMin 30 --outFilterMatchNmin 15`

Data Filtering, Normalisation, and Visualization

Preprocessing of the feature-count-matrix output by STARsolo was largely performed within the scanpy [67]ecosystem, with the exception of scran normalization [68], which was performed in R (R Core Team, 2017). All visualization was done using [69] functions. Default parameters were used unless detailed otherwise.

For wild type:
Barcodes with less than 3000 UMI were discarded.
Only barcodes with less than 15% of counts stemming from mitotic genes were retained.

For K14Cre-RBP-J floxed/floxed and control:
Barcodes with less than 2000 UMI were discarded.
Only barcodes with less than 20% of counts stemming from mitotic genes were retained.
Only barcodes with less than 70% of counts stemming from hemoglobin genes were retained.
And barcodes were filtered for a complexity value above 0.75, where complexity is defined as the log10-transformed number of expressed genes divided by the log10-transformed number of total counts per barcode. Scran was used for normalization.

The separate samples were merged into a single object, G2M and S phase scores were assigned to each cell using gene lists from [70] and the scanpy scanpy.tl.score_genes_cell_cycle function, and regressed out of the gene expression matrix using sc.pp.regress_out. 3000 highly variable genes were calculated from the normalized matrix (sc.pp.highly_variable_genes, flavor “seurat”), and the first 100 principal components were calculated with scanpy. Neighbourhood graph calculation (30 neighbors), UMAP dimensionality reduction [71], and Leiden clustering [72] were performed. scrublet [73] and/or scDblFinder were then used for doublet prediction.

Contaminant or undesired cell populations such as clusters of cells that, either manually or by scrublet/scDblFinder, could be classified as doublets based on their expression patterns, were removed. For this, cells were clustered at resolution 0.05, and the cluster corresponding to the

epidermal cells were isolated. These were then reclustered at resolution 0.1 (wild type) and 0.2 (K14Cre-RBP-J floxed/floxed) as described above, and undesired clusters were removed. Finally, PCA, nearest neighbor calculation, and UMAP dimensionality reduction were repeated for the clean epidermis data. For WT, stages E14.5, E15.5, and E16.5 were additionally analysed separately with batch-correction using Harmony [74] after cell-cycle regression.

Differential expression analysis

Differentially expressed genes were calculated using a pseudobulk approach [75], comparing aggregate counts with 2 pseudoreplicates for each condition (pyDeSEQ2 0.4.8).

Ligand-receptor interaction analysis

We used CellphoneDB (v2.1.7 [35] with default parameters to analyse ligand-receptor interactions. Mouse gene names were converted to human gene names prior to the analysis.

Gene Set Enrichment Analysis

We ranked differential expression results by pyDESeq2 shrunken log2-fold changes and used GSEApy (v1.0.6 [76]) "prerank" to calculate the enrichment statistics.

Imaging Mass Cytometry

Primary antibodies from bovine serum albumin (BSA)- and azide-free formulations were conjugated using the Maxpar X8 Labeling Kit (Standard BioTools) according to the manufacturer's protocol. Stainings were performed on frozen cryosections according to the manufacturer's protocol (Fluidigm). Briefly, 5 µm cryosections were prepared and stored at −80 °C until use. On the day of the experiment, slides were equilibrated at −20 °C for 1 h and then fixed in 4% paraformaldehyde (PFA) for 30 min at 4 °C. After washing in PBS, sections were incubated in blocking solution (3% BSA) for 45 min at room temperature, followed by incubation with the antibody cocktail prepared in 0.5% BSA for 1 h in a hydration chamber at room temperature. Slides were then rinsed in 0.2% Triton X-100/PBS, stained with Cell-ID Intercalator-IR (Fluidigm #201192A) for 30 min at room temperature, washed in Milli-Q water, air-dried for 30 min, and stored until imaging. The samples were laser-ablated at 200 Hz using a Hyperion imaging mass cytometry system (Fluidigm) coupled to a Helios time-of-flight mass cytometer with a resolution of 1 µm. Raw MiniCAD Design (MCD) files generated by the Hyperion Imaging System were first inspected using the MCD Viewer (Standard BioTools) to verify signal intensity and overall acquisition quality, and then exported as TIFF images

714 for downstream analysis on Image J. ROIs delineating the basement membrane were drawn, and
715 signal intensity at the basement membrane was measured using ImageJ software.
716
717 **Particle Imaging Velocimetry (PIV)**
718 PIV analysis of whole-embryo live imaging was performed as previously described, with minor
719 adjustments [13]. Briefly, prior to analysis, each movie was processed as follows: a 3D drift correction
720 was applied using the Fast4DReg plug-in in Fiji and sagittal cross-sections containing the basal
721 layers were selected. A median filter of 2 pixels was applied in Fiji, followed by background
722 subtraction using a rolling ball radius of 50 pixels.The movies were then imported into PIVLab
723 version 2.62. Tissue flow tracking was restricted to the interfollicular epidermis. To exclude the hair
724 follicle placodes from the analysis, ROIs covering the placodes were manually drawn on the raw
725 images and imported into PIVLab. These masks were overlaid onto the flow field to exclude the
726 placode regions. To prevent tracking errors due to intensity variations, image contrast was enhanced
727 using CLAHE (Contrast Limited Adaptive Histogram Equalization) with a box size of 64 pixels.
728 Denoising was performed using a Wiener Noise Filter with a maximum pixel count of 3. Tissue flow
729 tracking was carried out using a multi-pass, windowed FFT-based approach, with window sizes of 64
730 and 32 pixels for the first and second passes, respectively, and a 50% overlap. The resulting vector
731 fields were visually inspected, and any erroneous vectors were manually removed from the analysis.
732
733 **Culture of primary epidermal progenitor cells**
734 Primary epidermal cells were isolated from newborn mice essentially as described [13]. Briefly, after
735 dissection, skins were treated with antibiotic/antimycotic solution (Sigma A5955) for 5 min, and
736 epidermal single cell suspensions were generated by incubating skin pieces in 0.8% trypsin for
737 30 min at 37 °C. Cells were suspended in Keratinocyte Growth Medium (MEM Spinner's
738 modification (Sigma), 5 µg/ml insulin (Sigma), 10 ng/ml EGF (Sigma), 10 µg/ml transferrin (Sigma),
739 10 µM phosphoethanolamine (Sigma), 10 µM ethanolamine (Sigma), 0.36 µg ml/ml hydrocortisone
740 (Calbiochem), 2 mM glutamine (Gibco), 100 U ml/ml penicillin, 100 µg ml/ml streptomycin (Gibco),
741 10% chelated fetal calf serum (Gibco), 5 µM Y27632, 20 ng ml/ml mouse recombinant vascular
742 endothelial growth factor (VEGF) and 20 ng ml/ml human recombinant fibroblast growth factor-2
743 (FGF-2) (all from Miltenyi Biotec) and seeded on cell culture plates coated with 30 µg ml^{-1} collagen
744 I (Millipore) and 10 µg ml^{-1} fibronectin (Millipore) for 1 h at 37 °C.
745
746 **Micropatterned hydrogels**

747 Circular micropatterns (100 µm diameter) were generated on glass coverslips activated by oxygen
748 plasma treatment for 3 min (PDC-002-CE Expanded Plasma Cleaner), as described previously [9].
749 Activated coverslips were incubated with 1× PLL (Surface Solutions) for 30 min at room
750 temperature, rinsed with 10 mM HEPES (pH 7.8), and subsequently incubated with PEG-SVA (50
751 mg/ml in 10 mM HEPES, pH 7.8) for 1 h at room temperature. Coverslips were rinsed with Milli-Q
752 water and air-dried before patterning by deep-UV (Primo; Alveole). PEG-cleaved regions were
753 rinsed with Milli-Q water and incubated with 50 µg/ml fibronectin for 30 min at room temperature.
754 In parallel, glass-bottom plates (Ibidi, #81218-200) were silanized. Polyacrylamide gels of defined
755 stiffness were prepared by placing a drop of acrylamide/bis-acrylamide solution between the
756 micropatterned coverslip and the silanized plate. After 45 min of polymerization, the coverslip was
757 removed, transferring the ECM micropatterns onto the gel surface. Primary epidermal progenitors
758 were then seeded onto the patterned hydrogels.
759
760 **Live imaging of epidermal progenitor monolayers**
761 Freshly isolated epidermal progenitors isolated from N1IP: CreHI reporter mice crossed with
762 $R26R^{mT/mG}$ mice to label the plasma membrane and detect Cre activity were grown to confluency in
763 Keratinocyte Growth Medium and plated on 35 mm glass bottom dish with 14 mm micro-well plates
764 (Cellvis; D35-14-1.5-N). Upon confluency, 200 µM Ca^{2+} was added to induce differentiation.
765 Imaging was performed using an Andor Dragonfly 505 high-speed spinning disk confocal
766 microscope (Oxford Instruments) with an inverted Nikon Eclipse Ti2 microscope (Nikon) equipped
767 with 488 nm and 546 nm lasers, an Andor Zyla 4.2 sCMOS camera and an environmental chamber
768 set at 37°C, 5% CO2 using a 40X dry objective. Images were acquired using Fusion 2.0 software
769 (Andor) with multiple positions and drift stabilizer.

770

771 **Atomic Force Microscopy**

772 For Atomic Force Microscopy (AFM), embryonic skin was dissected, immediately nitrogen frozen
773 and then embedded in OCT blocks. AFM measurements of the basement membrane were performed
774 on freshly cut 20 µm-thick cryosections using JPK Nano Wizard IV (Bruker Nano) atomic force
775 microscope mounted on an Olympus IX73 inverted fluorescent microscopy (Olympus) and operated
776 via JPK SPM Control Software v.5. Cryosections were equilibrated in PBS supplemented with
777 protease inhibitors and measurements were performed within 20 minutes of thawing the samples.
778 Triangular non-conductive Silicon Nitride cantilevers (MLCT, Bruker Daltonics) with a nominal

779 spring constant of 0,07 Nm^{-1} were used for the nanoindentation experiments. For all indentation
780 experiments, forces of up to 3 nN were applied, and the velocities of cantilever approach and
781 retraction were kept constant at 10 μm^{s-1} ensuring an indentation depth of 500 nm. All analysis were
782 performed with JPK Data Processing Software (Bruker Nano). Prior to fitting the Hertz model
783 corrected by the tip geometry to obtain Young's Modulus (Poisson's ratio of 0.5), the offset was
784 removed from the baseline, contact point was identified, and the cantilever bending was subtracted
785 from all force curves. Force curves were filtered for quality and all valid forces curves were
786 analyzed.
787

788 **RNA in situ hybridization**

789 RNA in situ hybridization was performed using RNAscope technology according to the
790 manufacturer's instructions (ACD, RNAscope Multiplex Fluorescent v2 Assay, kit: RNAscope
791 Multiplex Fluorescent v2 Assay ACD, #323100). Briefly, paraffin-embedded tissue sections (5 µm
792 thick) were deparaffinized in xylene, rehydrated through an ethanol series, and incubated in hydrogen
793 peroxide for 10 min at RT. Sections were then subjected to antigen retrieval in RNAscope Target
794 Retrieval solution for 15 min at 100°C using a pressure cooker. RNAscope Protease Plus (ACD;
795 #322331) was applied to each section and incubated at 40°C for 30 min. The Eid1 RNAscope probe
796 (ACD; #1713581-C3) and Keratin-DAP RNAscope probe (ACD; #500671-C1) were hybridized
797 according to the manufacturer's protocol using the RNAscope Multiplex Fluorescent v2 Assay
798 (ACD; #323100), followed by signal detection with TSA Plus Fluorescein (Akoya,
799 #NEL741001KT), TSA Plus Cyanine 3 System (Akoya, #NEL744001KT). All hybridization and
800 amplification steps were performed in a HybEZ II oven (ACD). DAPI solution was incubated for 30
801 seconds at room temperature. Sections were mounted in Elvanol and imaged using a Zeiss LSM 980
802 confocal microscope equipped with a 40× water-immersion objective, using Zeiss ZEN software
803 (version 3.5).

804

805 **Statistics and reproducibility**

806 Statistical analyses were performed using GraphPad Prism software (GraphPad, version 9) or in R
807 (version 4.2.2). Statistical significance was determined by the specific tests indicated in the
808 corresponding figure legends. Only 2-tailed tests were used. In all cases where a test for normally
809 distributed data was used, normal distribution was confirmed with the Kolmogorov–Smirnov test (α

= 0.05). All experiments presented in the manuscript were repeated at least in 3 independent replicates.

Data availability

Sequencing datasets are available at GEO (GSE315748 and GSE315746). All analysis scripts, custom code, and data that support the conclusions are available from the authors on request.

Acknowledgements

We thank Claudia Ortmeier, Manuela Haustein, Hermann vom Bruch, and Sandra Heising for expert technical assistance, Silvia Fre (Institute Curie, France) for advice on the project and general support, Fabien Bertillot for advice on image analyses, Yekaterina Miroshnikova for advice on micropatterning, and the Max Planck Institute BioOptics and Sequencing core facilities for support with experiments. Imaging Mass Cytometry was performed at the Cell Imaging and Cytometry Core, Turku Bioscience Centre (Turku, Finland), with the support of Biocenter Finland. This work was supported by European Union's Horizon 2020 research and innovation programme under Marie Skłodowska-Curie grant agreement no. 101032331 (to CV), Research Council of Finland (332402) and The Turku Collegium for Science, Medicine, and Technology (to GF), Academy of Finland Center of Excellence BarrierForce (346131) and R'Life Programme consortium NucleoMech (330033) (to JI and SAW) the Sigrid Juselius Foundation, Helsinki Institute of Life Science, and the Max Planck Society (all to SAW), NSF-CMMI-1334611 (to SA and MLM), grant number 2023-329572 from the Chan Zuckerberg Initiative DAF, an advised fund of the Silicon Valley Community Foundation (to MLM), and the Syracuse University Office of Research Future Faculty Fellow Program (to SA). CMN is supported by the Deutsche Forschungsgemeinschaft (DFG, German Research Foundation: Germany´s Excellence Strategy – EXC 2030 – 390661388; SPP 1782 NI 1234/6-2, Project-ID 388932620; FOR 2743 NI 1234/7-1 Project-ID 678823; ANR/DFG NI 1234/9 (Project-ID 505673300) and the European Union NETSKINMODELS, COST Action no. CA21108.

Author contributions

CV, MA, and MR designed and performed experiments and analyzed data. SHAE and MLM developed vertex model and performed all simulations and analyses. KK analyzed sequencing data. SV and LCB supported live imaging and single cell sequencing experiments. AP performed and

841 analyzed immunofluorescence experiments, PZ assisted with imaging. GF and JI performed mass
842 cytometry experiment. CMN, MLM and SAW conceived and supervised the study, designed
843 experiments, and analyzed data. MLM and SAW wrote the paper. All authors commented and edited
844 the manuscript.

845

846 **Competing interests statement**

847 The authors declare no competing interests.

848

849 **References:**

850 1. Kulukian, A., and Fuchs, E. (2013). Spindle orientation and epidermal morphogenesis. Philos
851 Trans R Soc Lond B Biol Sci *368*, 20130016. 10.1098/rstb.2013.0016.
852 2. Niessen, C.M., Manning, M.L., and Wickstrom, S.A. (2025). Mechanochemical Principles of
853 Epidermal Tissue Dynamics. Cold Spring Harb Perspect Biol *17*.
854 10.1101/cshperspect.a041518.
855 3. Tai, K., Cockburn, K., and Greco, V. (2019). Flexibility sustains epithelial tissue homeostasis.
856 Curr Opin Cell Biol *60*, 84–91. 10.1016/j.ceb.2019.04.009.
857 4. Beumer, J., and Clevers, H. (2024). Hallmarks of stemness in mammalian tissues. Cell Stem
858 Cell *31*, 7–24. 10.1016/j.stem.2023.12.006.
859 5. Williams, S.E., and Fuchs, E. (2013). Oriented divisions, fate decisions. Curr Opin Cell Biol
860 *25*, 749–758. 10.1016/j.ceb.2013.08.003.
861 6. Damen, M., Wirtz, L., Soroka, E., Khatif, H., Kukat, C., Simons, B.D., and Bazzi, H. (2021).
862 High proliferation and delamination during skin epidermal stratification. Nat Commun *12*,
863 3227. 10.1038/s41467-021-23386-4.
864 7. Box, K., Joyce, B.W., and Devenport, D. (2019). Epithelial geometry regulates spindle
865 orientation and progenitor fate during formation of the mammalian epidermis. Elife *8*.
866 10.7554/eLife.47102.
867 8. Lechler, T., and Fuchs, E. (2005). Asymmetric cell divisions promote stratification and
868 differentiation of mammalian skin. Nature *437*, 275–280. 10.1038/nature03922.
869 9. Miroshnikova, Y.A., Le, H.Q., Schneider, D., Thalheim, T., Rubsam, M., Bremicker, N.,
870 Polleux, J., Kamprad, N., Tarantola, M., Wang, I., et al. (2018). Adhesion forces and cortical
871 tension couple cell proliferation and differentiation to drive epidermal stratification. Nat Cell
872 Biol *20*, 69–80. 10.1038/s41556-017-0005-z.
873 10. Williams, S.E., Ratliff, L.A., Postiglione, M.P., Knoblich, J.A., and Fuchs, E. (2014). Par3-
874 mInsc and Galphai3 cooperate to promote oriented epidermal cell divisions through LGN. Nat
875 Cell Biol *16*, 758–769. 10.1038/ncb3001.
876 11. Cockburn, K., Annusver, K., Gonzalez, D.G., Ganesan, S., May, D.P., Mesa, K.R.,
877 Kawaguchi, K., Kasper, M., and Greco, V. (2022). Gradual differentiation uncoupled from
878 cell cycle exit generates heterogeneity in the epidermal stem cell layer. Nat Cell Biol *24*,
879 1692–1700. 10.1038/s41556-022-01021-8.
880 12. Mesa, K.R., Kawaguchi, K., Cockburn, K., Gonzalez, D., Boucher, J., Xin, T., Klein, A.M.,
881 and Greco, V. (2018). Homeostatic Epidermal Stem Cell Self-Renewal Is Driven by Local
882 Differentiation. Cell Stem Cell *23*, 677–686 e674. 10.1016/j.stem.2018.09.005.

13. Villeneuve, C., Hashmi, A., Ylivinkka, I., Lawson-Keister, E., Miroshnikova, Y.A., Perez-Gonzalez, C., Myllymaki, S.M., Bertillot, F., Yadav, B., Zhang, T., et al. (2024). Mechanical forces across compartments coordinate cell shape and fate transitions to generate tissue architecture. Nat Cell Biol *26*, 207–218. 10.1038/s41556-023-01332-4.
14. Moll, R., Franke, W.W., Schiller, D.L., Geiger, B., and Krepler, R. (1982). The catalog of human cytokeratins: patterns of expression in normal epithelia, tumors and cultured cells. Cell *31*, 11–24. 10.1016/0092-8674(82)90400-7.
15. Nekrasova, O., Harmon, R.M., Broussard, J.A., Koetsier, J.L., Godsel, L.M., Fitz, G.N., Gardel, M.L., and Green, K.J. (2018). Desmosomal cadherin association with Tctex-1 and cortactin-Arp2/3 drives perijunctional actin polymerization to promote keratinocyte delamination. Nat Commun *9*, 1053. 10.1038/s41467-018-03414-6.
16. Zhang, T., and Schwarz, J.M. (2022). Topologically-protected interior for three-dimensional confluent cellular collectives. Physical Review Research *4*, 043148. 10.1103/PhysRevResearch.4.043148.
17. Sahu, P., Monteiro-Ferreira, S., Canato, S., Soares, R.M., Sanchez-Danes, A., and Hannezo, E. (2025). Mechanical control of cell fate decisions in the skin epidermis. Nat Commun *16*, 8440. 10.1038/s41467-025-62882-9.
18. Fukamachi, S., Datta, R., Wuergezhen, D., Ichikawa, T., Yagasaki, R., Horiguchi, S.A., Leeaw, P., Omachi, K., Sada, A., Imayoshi, I., et al. (2024). Epithelium Stratifies via Nucleation and Growth Induced by Foam-Geometric Instability. bioRxiv, 2024.2012.2026.630435. 10.1101/2024.12.26.630435.
19. Bi, D., Lopez, J.H., Schwarz, J.M., and Manning, M.L. (2015). A density-independent rigidity transition in biological tissues. Nature Physics *11*, 1074–1079. 10.1038/nphys3471.
20. Merkel, M., and Manning, M.L. (2018). A geometrically controlled rigidity transition in a model for confluent 3D tissues. New Journal of Physics *20*, 022002. 10.1088/1367-2630/aaaa13.
21. Okuda, S., and Fujimoto, K. (2020). A Mechanical Instability in Planar Epithelial Monolayers Leads to Cell Extrusion. Biophysical Journal *118*, 2549–2560. https://doi.org/10.1016/j.bpj.2020.03.028.
22. Devany, J., Sussman, D.M., Yamamoto, T., Manning, M.L., and Gardel, M.L. (2021). Cell cycle-dependent active stress drives epithelia remodeling. Proc Natl Acad Sci U S A *118*. 10.1073/pnas.1917853118.
23. Erdemci-Tandogan, G., Clark, M.J., Amack, J.D., and Manning, M.L. (2018). Tissue Flow Induces Cell Shape Changes During Organogenesis. Biophys J *115*, 2259–2270. 10.1016/j.bpj.2018.10.028.
24. Serwane, F., Mongera, A., Rowghanian, P., Kealhofer, D.A., Lucio, A.A., Hockenbery, Z.M., and Campas, O. (2017). In vivo quantification of spatially varying mechanical properties in developing tissues. Nat Methods *14*, 181–186. 10.1038/nmeth.4101.
25. Somendra, M.B., and Flavio, S. (2001). A measure of data collapse for scaling. Journal of Physics A: Mathematical and General *34*, 6375. 10.1088/0305-4470/34/33/302.
26. Bi, D., Lopez, J.H., Schwarz, J.M., and Manning, M.L. (2014). Energy barriers and cell migration in densely packed tissues. Soft Matter *10*, 1885–1890. 10.1039/c3sm52893f.
27. McQuarrie, D.A. (1976). Statistical Mechanics (Harper & Row).
28. Mombach, J.C.M., Robert D. , Graner, F., Gillet, G., Thomas, G.L., Idiart, M., and Rieu, J.P. (2005). Rounding of aggregates of biological cells: Experiments and simulations. Physica A: Statistical Mechanics and its Applications *352* (*525*). 10.1016/j.physa.2005.02.008.
29. Maitre, J.L., Berthoumieux, H., Krens, S.F., Salbreux, G., Julicher, F., Paluch, E., and Heisenberg, C.P. (2012). Adhesion functions in cell sorting by mechanically coupling the cortices of adhering cells. Science *338*, 253–256. 10.1126/science.1225399.

30. Pawlizak, S., Fritsch, A.W., Grosser, S., Ahrens, D., Thalheim, T., Riedel, S., Kießling, T.R., Oswald, L., Zink, M., Manning, M.L., and Käs, J.A. (2015). Testing the differential adhesion hypothesis across the epithelial−mesenchymal transition. New Journal of Physics *17*, 083049. 10.1088/1367-2630/17/8/083049.
31. Sahu, P., Schwarz, J.M., and Manning, M.L. (2021). Geometric signatures of tissue surface tension in a three-dimensional model of confluent tissue. New Journal of Physics *23*, 093043. 10.1088/1367-2630/ac23f1.
32. Sahu, P., Sussman, D.M., Rübsam, M., Mertz, A.F., Horsley, V., Dufresne, E.R., Niessen, C.M., Marchetti, M.C., Manning, M.L., and Schwarz, J.M. (2020). Small-scale demixing in confluent biological tissues. Soft Matter *16*, 3325–3337. 10.1039/C9SM01084J.
33. Press, W.H., Teukolsky, S.A., Vetterling, W.T., and Flannery, B.P. (2020). Numerical Recipes: The Art of Scientific Computing (Cambridge University Press).
34. Blanpain, C., Lowry, W.E., Pasolli, H.A., and Fuchs, E. (2006). Canonical notch signaling functions as a commitment switch in the epidermal lineage. Genes Dev *20*, 3022–3035. 10.1101/gad.1477606.
35. Efremova, M., Vento-Tormo, M., Teichmann, S.A., and Vento-Tormo, R. (2020). CellPhoneDB: inferring cell-cell communication from combined expression of multi-subunit ligand-receptor complexes. Nat Protoc *15*, 1484–1506. 10.1038/s41596-020-0292-x.
36. Giesen, C., Wang, H.A., Schapiro, D., Zivanovic, N., Jacobs, A., Hattendorf, B., Schuffler, P.J., Grolimund, D., Buhmann, J.M., Brandt, S., et al. (2014). Highly multiplexed imaging of tumor tissues with subcellular resolution by mass cytometry. Nat Methods *11*, 417–422. 10.1038/nmeth.2869.
37. Röper, K. (2012). Anisotropy of Crumbs and aPKC Drives Myosin Cable Assembly during Tube Formation. Developmental Cell *23*, 939–953. 10.1016/j.devcel.2012.09.013.
38. Rustarazo-Calvo, L., Pallares-Cartes, C., Aguirre-Tamaral, A., Floris, E., Hingerl, M., Autorino, C., Maula Khan, A.U., Corominas-Murtra, B., and Petridou, N.I. (2025). Adhesion-driven tissue rigidification triggers epithelial cell polarity. bioRxiv, 2025.2003.2018.644006. 10.1101/2025.03.18.644006.
39. Liu, Z., Turkoz, A., Jackson, E.N., Corbo, J.C., Engelbach, J.A., Garbow, J.R., Piwnica-Worms, D.R., and Kopan, R. (2011). Notch1 loss of heterozygosity causes vascular tumors and lethal hemorrhage in mice. J Clin Invest *121*, 800–808. 10.1172/JCI43114.
40. Hafner, M., Wenk, J., Nenci, A., Pasparakis, M., Scharffetter-Kochanek, K., Smyth, N., Peters, T., Kess, D., Holtkotter, O., Shephard, P., et al. (2004). Keratin 14 Cre transgenic mice authenticate keratin 14 as an oocyte-expressed protein. Genesis *38*, 176–181. 10.1002/gene.20016.
41. Tanigaki, K., Han, H., Yamamoto, N., Tashiro, K., Ikegawa, M., Kuroda, K., Suzuki, A., Nakano, T., and Honjo, T. (2002). Notch-RBP-J signaling is involved in cell fate determination of marginal zone B cells. Nat Immunol *3*, 443–450. 10.1038/ni793.
42. Lin, L., DeMartino, J., Wang, D., van Son, G.J.F., van der Linden, R., Begthel, H., Korving, J., Andersson-Rolf, A., van den Brink, S., Lopez-Iglesias, C., et al. (2023). Unbiased transcription factor CRISPR screen identifies ZNF800 as master repressor of enteroendocrine differentiation. Science *382*, 451–458. 10.1126/science.adi2246.
43. Miyake, S., Sellers, W.R., Safran, M., Li, X., Zhao, W., Grossman, S.R., Gan, J., DeCaprio, J.A., Adams, P.D., and Kaelin, W.G., Jr. (2000). Cells degrade a novel inhibitor of differentiation with E1A-like properties upon exiting the cell cycle. Mol Cell Biol *20*, 8889–8902. 10.1128/MCB.20.23.8889-8902.2000.
44. Witte, S., Bradley, A., Enright, A.J., and Muljo, S.A. (2015). High-density P300 enhancers control cell state transitions. BMC Genomics *16*, 903. 10.1186/s12864-015-1905-6.
45. Andrews, T.G.R., Cornwall-Scoones, J., Ramel, M.-C., Gupta, K., Briscoe, J., and Priya, R. (2025). Mechanochemical coupling of cell shape and organ function optimizes heart size and

contractile efficiency in zebrafish. Developmental Cell *60*, 3167–3184.e3168. 10.1016/j.devcel.2025.07.011.

46. Priya, R., Allanki, S., Gentile, A., Mansingh, S., Uribe, V., Maischein, H.M., and Stainier, D.Y.R. (2020). Tension heterogeneity directs form and fate to pattern the myocardial wall. Nature *588*, 130–134. 10.1038/s41586-020-2946-9.

47. Khait, I., Orsher, Y., Golan, O., Binshtok, U., Gordon-Bar, N., Amir-Zilberstein, L., and Sprinzak, D. (2016). Quantitative Analysis of Delta-like 1 Membrane Dynamics Elucidates the Role of Contact Geometry on Notch Signaling. Cell Rep *14*, 225–233. 10.1016/j.celrep.2015.12.040.

48. Shaya, O., Binshtok, U., Hersch, M., Rivkin, D., Weinreb, S., Amir-Zilberstein, L., Khamaisi, B., Oppenheim, O., Desai, R.A., Goodyear, R.J., et al. (2017). Cell-Cell Contact Area Affects Notch Signaling and Notch-Dependent Patterning. Dev Cell *40*, 505–511 e506. 10.1016/j.devcel.2017.02.009.

49. Sarate, R.M., Hochstetter, J., Valet, M., Hallou, A., Song, Y., Bansaccal, N., Ligare, M., Aragona, M., Engelman, D., Bauduin, A., et al. (2024). Dynamic regulation of tissue fluidity controls skin repair during wound healing. Cell *187*, 5298–5315.e5219. 10.1016/j.cell.2024.07.031.

50. Hogg, S.J., Motorna, O., Cluse, L.A., Johanson, T.M., Coughlan, H.D., Raviram, R., Myers, R.M., Costacurta, M., Todorovski, I., Pijpers, L., et al. (2021). Targeting histone acetylation dynamics and oncogenic transcription by catalytic P300/CBP inhibition. Mol Cell *81*, 2183–2200 e2113. 10.1016/j.molcel.2021.04.015.

51. Weinert, B.T., Narita, T., Satpathy, S., Srinivasan, B., Hansen, B.K., Scholz, C., Hamilton, W.B., Zucconi, B.E., Wang, W.W., Liu, W.R., et al. (2018). Time-Resolved Analysis Reveals Rapid Dynamics and Broad Scope of the CBP/p300 Acetylome. Cell *174*, 231–244 e212. 10.1016/j.cell.2018.04.033.

52. Pylvanainen, J.W., Laine, R.F., Saraiva, B.M.S., Ghimire, S., Follain, G., Henriques, R., and Jacquemet, G. (2023). Fast4DReg - fast registration of 4D microscopy datasets. J Cell Sci *136*. 10.1242/jcs.260728.

53. Pachitariu, M., Rariden, M., and Stringer, C. (2025). Cellpose-SAM: superhuman generalization for cellular segmentation. bioRxiv, 2025.2004.2028.651001. 10.1101/2025.04.28.651001.

54. Shen, L., Farid, H., and McPeek, M.A. (2009). Modeling three-dimensional morphological structures using spherical harmonics. Evolution *63*, 1003–1016. 10.1111/j.1558-5646.2008.00557.x.

55. Biggs, L.C., Kim, C.S., Miroshnikova, Y.A., and Wickstrom, S.A. (2020). Mechanical Forces in the Skin: Roles in Tissue Architecture, Stability, and Function. J Invest Dermatol *140*, 284–290. 10.1016/j.jid.2019.06.137.

56. Dahmann, C., Oates, A.C., and Brand, M. (2011). Boundary formation and maintenance in tissue development. Nat Rev Genet *12*, 43–55. 10.1038/nrg2902.

57. Foty, R.A., and Steinberg, M.S. (2005). The differential adhesion hypothesis: a direct evaluation. Dev Biol *278*, 255–263. 10.1016/j.ydbio.2004.11.012.

58. Harris, T.J., and Tepass, U. (2010). Adherens junctions: from molecules to morphogenesis. Nat Rev Mol Cell Biol *11*, 502–514. 10.1038/nrm2927.

59. Joost, S., Zeisel, A., Jacob, T., Sun, X., La Manno, G., Lonnerberg, P., Linnarsson, S., and Kasper, M. (2016). Single-Cell Transcriptomics Reveals that Differentiation and Spatial Signatures Shape Epidermal and Hair Follicle Heterogeneity. Cell Syst *3*, 221–237 e229. 10.1016/j.cels.2016.08.010.

60. Krieg, M., Arboleda-Estudillo, Y., Puech, P.H., Kafer, J., Graner, F., Muller, D.J., and Heisenberg, C.P. (2008). Tensile forces govern germ-layer organization in zebrafish. Nat Cell Biol *10*, 429–436. 10.1038/ncb1705.

61. Monier, B., Pelissier-Monier, A., Brand, A.H., and Sanson, B. (2010). An actomyosin-based barrier inhibits cell mixing at compartmental boundaries in Drosophila embryos. Nat Cell Biol *12*, 60–69. 10.1038/ncb2005.
62. Rubsam, M., Broussard, J.A., Wickstrom, S.A., Nekrasova, O., Green, K.J., and Niessen, C.M. (2018). Adherens Junctions and Desmosomes Coordinate Mechanics and Signaling to Orchestrate Tissue Morphogenesis and Function: An Evolutionary Perspective. Cold Spring Harb Perspect Biol *10*. 10.1101/cshperspect.a029207.
63. Wickstrom, S.A., and Niessen, C.M. (2018). Cell adhesion and mechanics as drivers of tissue organization and differentiation: local cues for large scale organization. Curr Opin Cell Biol *54*, 89–97. 10.1016/j.ceb.2018.05.003.
64. Watt, F.M. (2002). Role of integrins in regulating epidermal adhesion, growth and differentiation. The EMBO Journal *21*, 3919–3926. 10.1093/emboj/cdf399.
65. Sugimoto, M., Tada, Y., Shichino, S., Koyamatsu, S., Tsumaki, N., and Abe, K. (2022). Universal Surface Biotinylation: a simple, versatile and cost-effective sample multiplexing method for single-cell RNA-seq analysis. DNA Res *29*. 10.1093/dnares/dsac017.
66. Dobin, A., Davis, C.A., Schlesinger, F., Drenkow, J., Zaleski, C., Jha, S., Batut, P., Chaisson, M., and Gingeras, T.R. (2013). STAR: ultrafast universal RNA-seq aligner. Bioinformatics *29*, 15–21. 10.1093/bioinformatics/bts635.
67. Wolf, F.A., Angerer, P., and Theis, F.J. (2018). SCANPY: large-scale single-cell gene expression data analysis. Genome Biol *19*, 15. 10.1186/s13059-017-1382-0.
68. Lun, A.T., Bach, K., and Marioni, J.C. (2016). Pooling across cells to normalize single-cell RNA sequencing data with many zero counts. Genome Biol *17*, 75. 10.1186/s13059-016-0947-7.
69. Hunter, J.D. (2007). Matplotlib: A 2D Graphics Environment. Computing in Science & Engineering *9*, 90–95. 10.1109/MCSE.2007.55.
70. Tirosh, I., Izar, B., Prakadan, S.M., Wadsworth, M.H., 2nd, Treacy, D., Trombetta, J.J., Rotem, A., Rodman, C., Lian, C., Murphy, G., et al. (2016). Dissecting the multicellular ecosystem of metastatic melanoma by single-cell RNA-seq. Science *352*, 189–196. 10.1126/science.aad0501.
71. McInnes, L.H., J.; Melville, J. (2020). UMAP: Uniform Manifold Approximation and Projection for Dimension Reduction. https://arxiv.org/abs/1802.03426}, .
72. Traag, V.A., Waltman, L., and van Eck, N.J. (2019). From Louvain to Leiden: guaranteeing well-connected communities. Sci Rep *9*, 5233. 10.1038/s41598-019-41695-z.
73. Wolock, S.L., Lopez, R., and Klein, A.M. (2019). Scrublet: Computational Identification of Cell Doublets in Single-Cell Transcriptomic Data. Cell Systems *8*, 281–291.e289. https://doi.org/10.1016/j.cels.2018.11.005.
74. Korsunsky, I., Millard, N., Fan, J., Slowikowski, K., Zhang, F., Wei, K., Baglaenko, Y., Brenner, M., Loh, P.R., and Raychaudhuri, S. (2019). Fast, sensitive and accurate integration of single-cell data with Harmony. Nat Methods *16*, 1289–1296. 10.1038/s41592-019-0619-0.
75. Squair, J.W., Gautier, M., Kathe, C., Anderson, M.A., James, N.D., Hutson, T.H., Hudelle, R., Qaiser, T., Matson, K.J.E., Barraud, Q., et al. (2021). Confronting false discoveries in single-cell differential expression. Nat Commun *12*, 5692. 10.1038/s41467-021-25960-2.
76. Fang, Z., Liu, X., and Peltz, G. (2023). GSEApy: a comprehensive package for performing gene set enrichment analysis in Python. Bioinformatics *39*. 10.1093/bioinformatics/btac757.

Main Figures

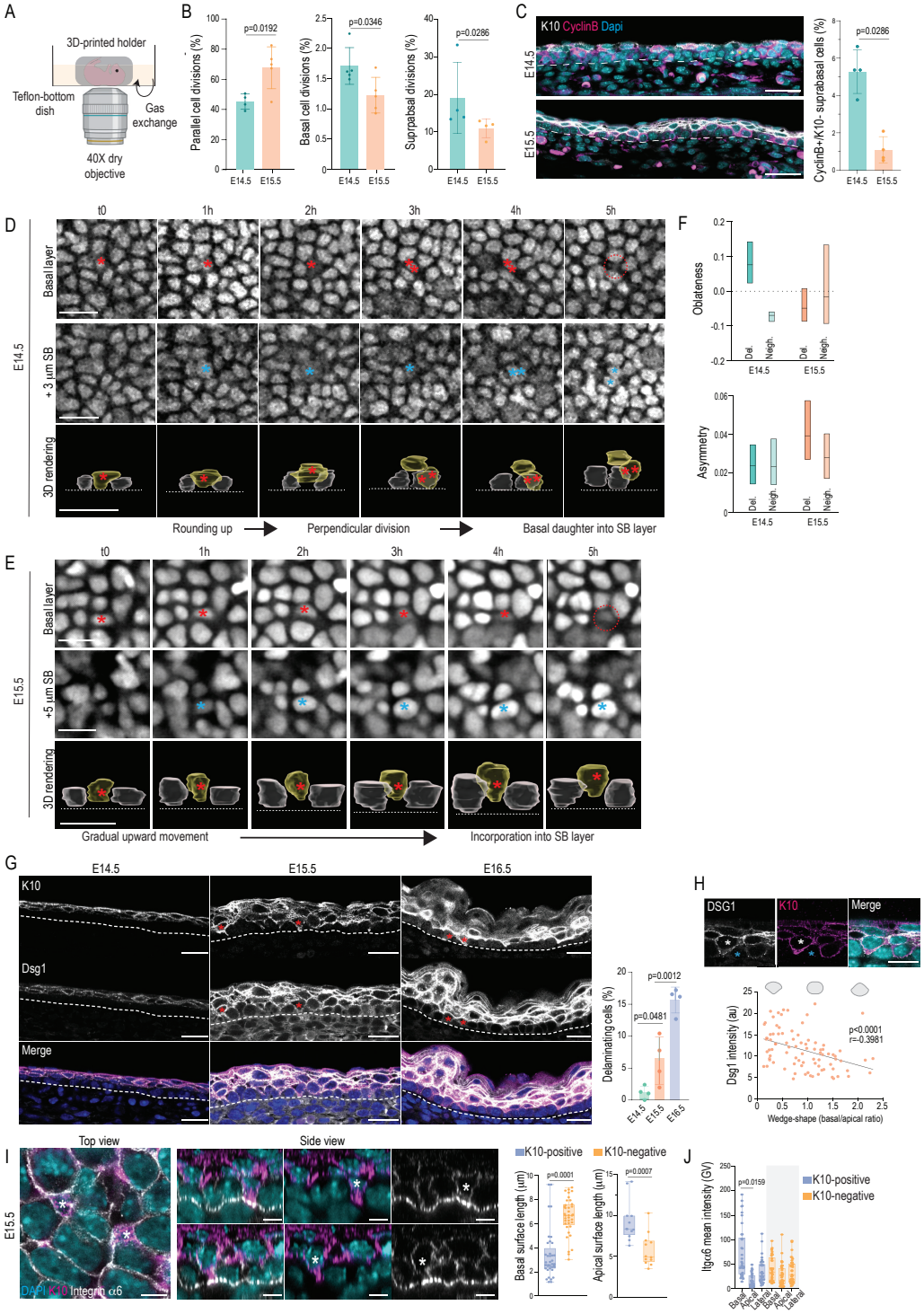

Figure 1. Basal cells employ distinct embryonic stage-specific strategies to generate suprabasal layers

A. Schematics of the *ex vivo* embryo imaging setup. **B.** Quantification of parallel (left panel), basal (middle panel) and suprabasal (right panel) cell divisions in E14.5 and E15.5 embryos (mean ±SD; n=4 (E14.5) /5 (E15.5) embryos; Student's t-test (left and middle panel), Mann-Whitney (right

panel)). **C.** Representative images and quantification of CyclinB-positive undifferentiated cells (K10-neg) in the suprabasal layers of E14.5 and E15.5 embryos (30 µm; mean ±SD; n=4 embryos/stage; Mann-Whitney). **D.** Representative snapshots and 3D rendering (lower panel) from live imaging movies of E14.5 epidermis from nTomato reporter mice. Red asterisk marks cell departing from basal layer; double red asterisk marks daughter of perpendicular division that subsequently moves suprabasally, blue asterisks marks appearance of cells in the suprabasal layer, red dotted circle marks completed delamination. Images representative of 3 embryos, scale bars 20 µm. **E.** Representative snapshots and 3D rendering (lower panel) from live imaging movies of E15.5 epidermis from nTomato reporter mice. Red asterisk marks cell departing from basal layer; blue asterisk marks appearance of this cell in the suprabasal layer, red dotted circle marks completed delamination. Images representative of 3 embryos, scale bars 20 µm. **F.** Quantification of nuclear oblateness (roundness; upper panel) and asymmetry of deformation (wedge-shape; lower panel) of delaminating cells (Del.) and their immediate neighbors (Neigh.) from 3D renderings. Note that while at E14.5 delaminating cells round up, at E15.5 they elongate in an asymmetric manner (min-to-max box plots; n=3 embryos/stage). **G.** Representative images and quantification of tissue sections from E14.5 - 16.5 embryos stained against K10, Dsg1 and DAPI. Note emergence of K10-Dsg1- positive cells at 15.5 (red asterisks). Dotted line marks basement membrane (scale bars 20 µm; mean ±SD; n=4 embryos; Two-way ANOVA/Tukey's). **H.** Representative images and quantification of tissue sections from E15.5 embryos stained against K10, Dsg1 and DAPI. Note correlation of wedge-like shape and apical Dsg1 intensity. White asterisks mark wedge-like cells with high apical Dsg1, blue asterisks mark cuboidal neighboring cell (scale bars 10 µm; mean ±SD; n=87 cells pooled across 3 embryos; Simple linear regression; Pearson's correlation). **I, J.** Representative images and quantification of delaminating cells in E15.5 embryo 3D whole mounts stained against integrin α6 (Itga6), K10 and DAPI. Note wedge-like shape and integrin α6-positive basal footprint of the delaminating cell (white asterisks; scale bars 5 µm; min-max box and whiskers; n=37 cells pooled across 3 embryos; Mann-Whitney (left, middle panel) Friedman/Dunn's).

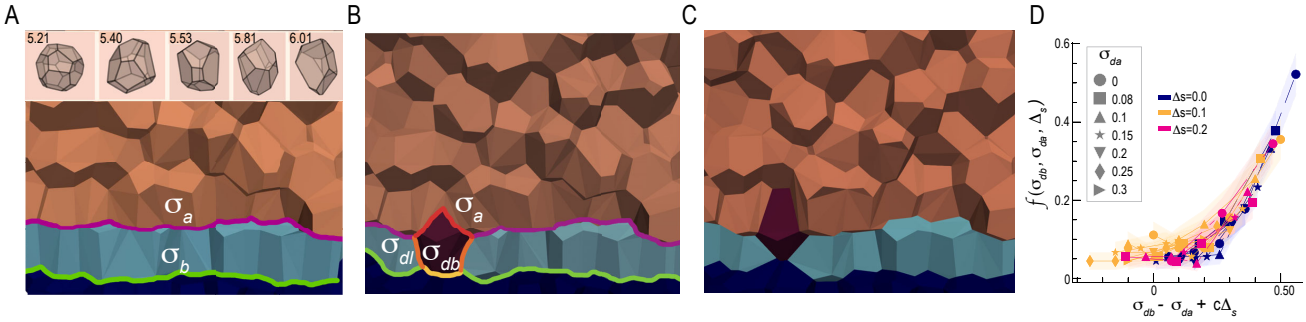

Figure 2. A biophysical model predicts that in the presence of a mechanical barrier, delamination depends on the mechanical properties of the delaminating cell.

A. Snapshot from 3D vertex model for stratified epithelium geometry, illustrating suprabasal cells (brown), basal cells (light blue) and basement membrane (dark blue), interfacial tensions between the apical surface of basal cells and the adjacent suprabasal cell (, magenta), basal cells and basement membrane (σ_b, green), and cell shapes (inset) with different 3D shape parameters. **B.** Simulation snapshot including a delaminating cell type, with potentially different delaminating cell-basal cell lateral interfaces σ_{dl}, delaminating cell-basement membrane interfaces (σ_b, yellow), and delaminating cell-suprabasal cell interfaces (σ_{da}, red). **C.** Snapshot of simulation showing cell in process of delaminating (cell integrates fully into the suprabasal layer by end of simulation). **D.** Fraction of cells that delaminate after a time t = X, as a function of σ_{db}, for many different values of the other parameters. Data averaged over an ensemble of n=20 simulations for each simulation condition. **E.** Delamination fraction collapses as a specific function of vertex model parameters.

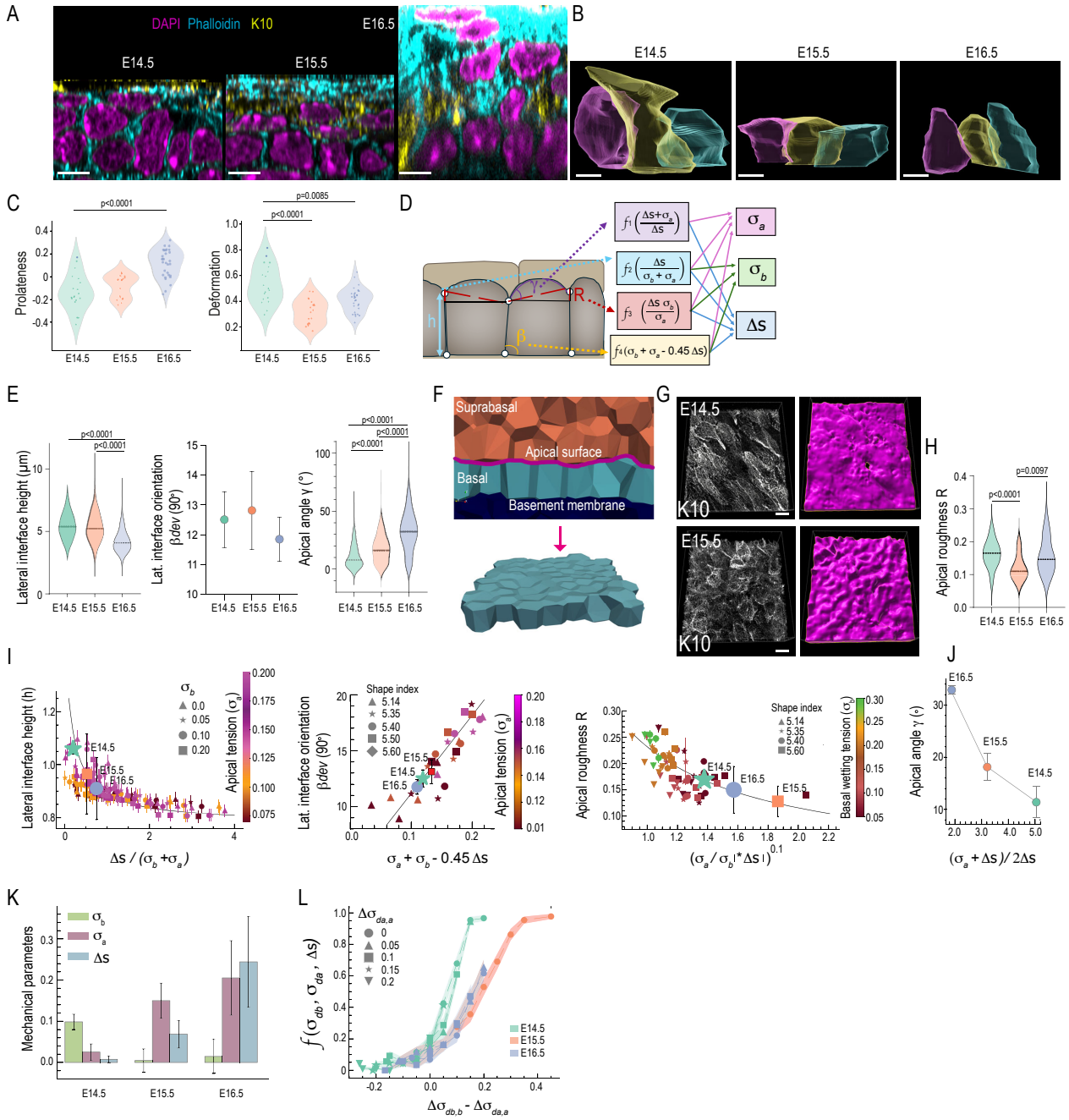

Figure 3. A mechanical boundary emerges at E15.5 impacting delamination.

A. Representative super resolution images of tissue cross sections across developmental stages. Scale bars 10 µm. **B.** 3D rendering of cell shapes across developmental stages from data in (A). Scale bars 5µm. **C.** Quantification of 3D cell shapes from (B) using spherical harmonics reveals a decrease in deformed shapes and an increase in prolateness from E14.5 to E16.5 (n=19 (E14.5, E15.5)/ 30 (E16.5) cells pooled across 3 embryos; Kruskal-Wallis/Dunn's). **D.** Schematic representation of cell-scale geometric parameters and their integration into the vertex model. **E.** Quantification of lateral interface height, variability of orientation angle and apical surface angle across developmental stages

(n>400 cells (height); >25 fields of view (apical angle) >740 cells (lateral angle) per timepoint pooled across 3 mice (E14.5, E15.4), 5 mice (E15.5); Kruskal-Wallis/Dunn's). **F.** Schematic representation of tissue-scale geometric parameter of surface roughness in the 3D vertex model. **G, H.** Representative experimental whole mount (B) and cross section images (C) of surface roughness measurements (scale bars 10 µm). **I.** Collapsed simulation data measured in the 3D model simulations across mechanical parameter space ($\sigma_a, \sigma_b, \Delta s$). Corresponding averages of *in vivo* observables converted to simulation units specified as green, orange and blue symbols (n>85 simulations for each parameter set). **J.** Apical angle simulation data as a function of vertex model parameters required by force balance (n>85 simulations for each parameter set). **K.** Best-fit vertex model parameters σ_b (green), σ_a (pink), Δs (blue) to the cell and tissue geometry observed at each stage; error bars represent uncertainty in the fit (see Supplemental Methods). **L.** Simulation-predicted delamination rates when delaminating cells alter their mechanical properties from the background basal cells by $\Delta\sigma_{da,a}$ (apical) and $\Delta\sigma_{db,b}$ (basal). Rate is the fraction that delaminates in a fixed time window t = 2000 timesteps, corresponding to τ ~ 20 simulation time units (n>85 simulations per parameter set).

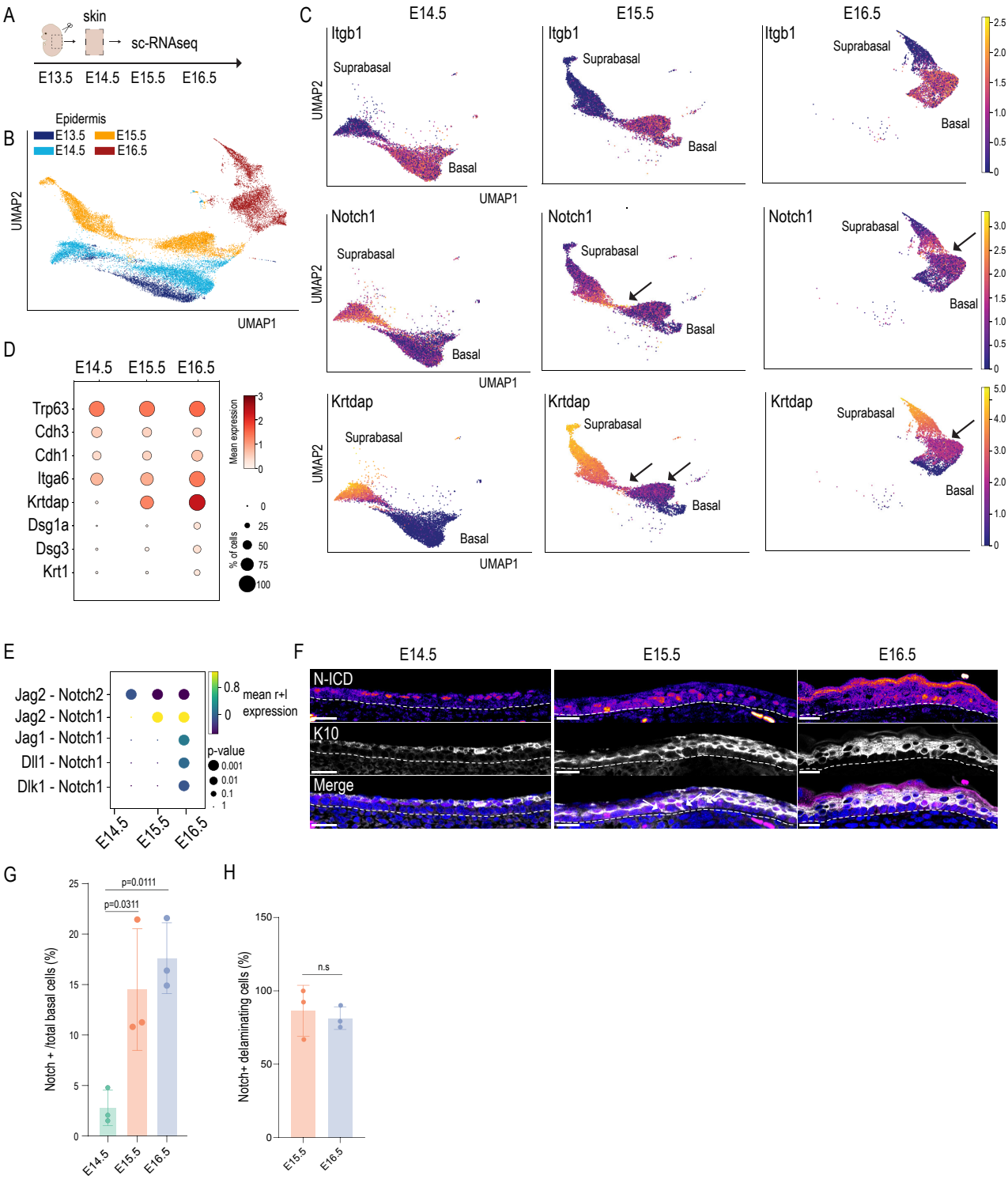

Figure 4. A committed basal population characterized by Notch activation emerges at E15.5

A. Schematics of the scRNAseq experiment. **B.** UMAP representation of the Leiden clusters of filtered epidermal cells from scRNAseq. Embryonic stages of cells are color coded. **C.** UMAP projections of basal identity and differentiation gene expression across E14.5-E16.5. Arrowheads mark transition population between basal and suprabasal cells. **D.** Dotplot of selected genes across

1157 E14.5-E16.5 basal cells. Note increased expression of differentiation genes in basal cells of E15.5
1158 and E16.5 embryos. **E.** Dot plot of receptor-ligand (r+l) analyses between basal stem cells across
1159 E14.5-E16.5. Note increased predicted Jag2-Notch signaling interaction at E15.5 and E16.5. **F-H.**
1160 Representative images (F) and quantification (G, H) of tissue sections from E14.5- 16.5 embryos
1161 stained against Notch intracellular domain (N-ICD) and K10. Note emergence of N-ICD-K10-
1162 positive delaminating basal cells at 15.5. Dotted line marks basement membrane (mean ±SD; scale
1163 bars 20 µm; n=3 embryos/stage; Two-way ANOVA/Tukey's (G); Mann-Whitney (H)).

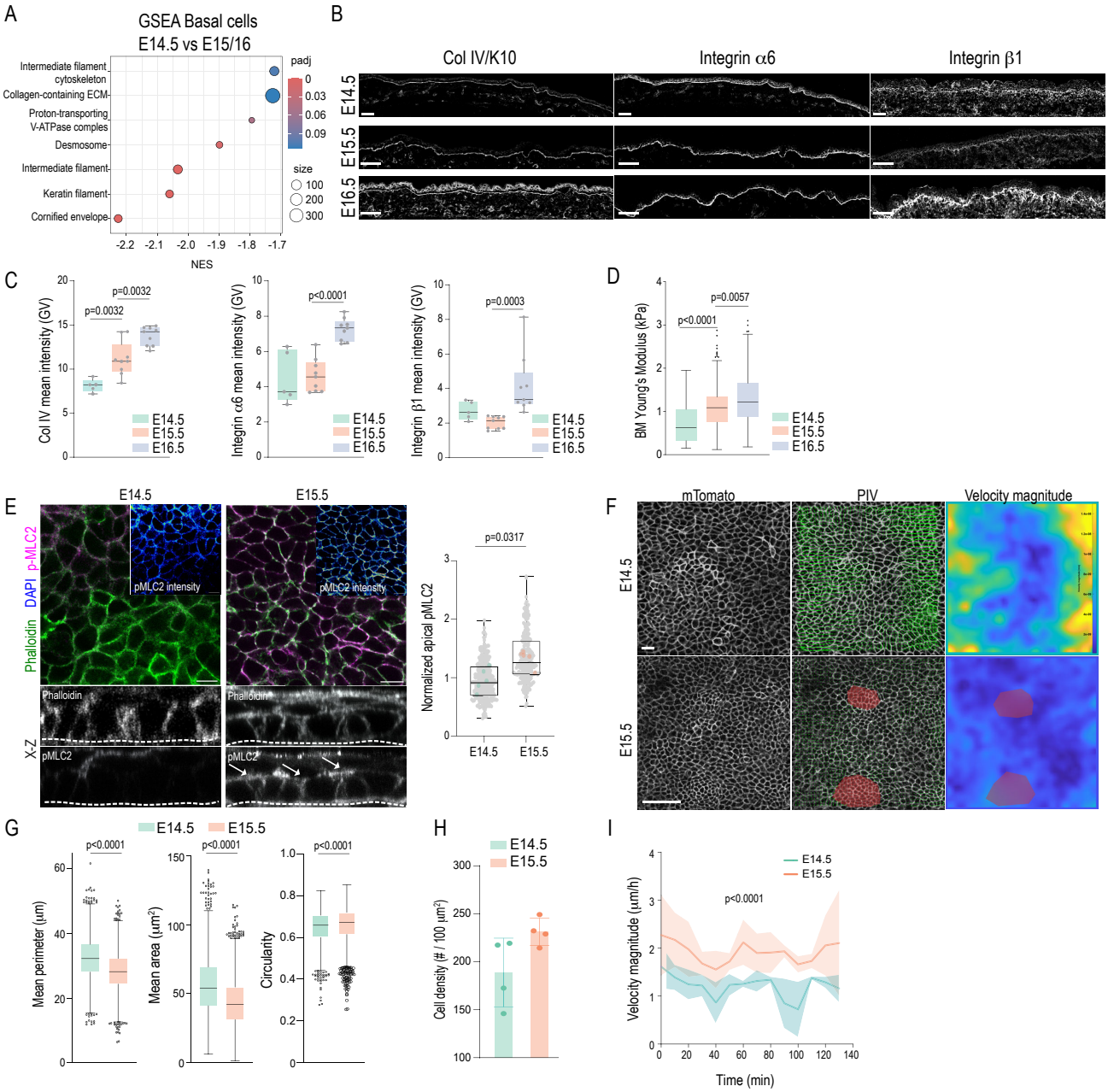

1164

1165 **Figure 5. Generation of the mechanical boundary at E15.5 is concomitant with stiffening of the**
1166 **basement membrane and rigidification of the basal layer**

1167 **A.** Dot plot of Gene set enrichment analyses (GSEA) from differentially expressed genes in basal
1168 cells of E14.5 versus E15.5/E16.5 embryos from scRNAseq data. **B, C.** Representative images (B)
1169 and quantification (C) of tissue sections from E14.5- 16.5 embryos analyzed by mass cytometry.
1170 Note increased expression of basement membrane Collagen IV (counterstained with K10) and
1171 integrins α6 and β1 (mean ±SD; scale bars 50 µm; n=3 embryos/stage; Two-way ANOVA/Tukey's
1172 (Left and middle panel), Kruskal-Wallis/Dunn's (right panel)). **D.** Basement membrane Young's
1173 moduli extracted from AFM force indentation experiments (Tukey's box and whiskers; n>200 force
1174 curves pooled across 3embryos/stage; Kolmogorov-Smirnov). **E.** Representative images and
1175 quantification of skin wholemounts from E14.5 and E15.5 embryos stained for pMLC2 and
1176 phalloidin. Note increased pMLC2 intensity at cell junctions and interface between basal and
1177 suprabasal layers (arrows) (min-max box and whiskers; scale bars 10 µm; n=5 embryos/stage; Mann-
1178 Whitney)**. F.** Representative snapshots from live imaging movies and subsequent PIV analyses of
1179 velocity magnitudes of E14.5 and E15.5 epidermis from membrane-Tomato (mTomato) reporter
1180 mice. Red masks mark excluded hair follicle areas (scale bars 50 µm). **G.** Quantification of 2D cell
1181 perimeter, area and circularity from data in (A) (Tukey's box and whiskers; n>2300 cells pooled
1182 across 3 embryos/stage; Mann-Whitney). **H.** Quantification of cell densities from data in (A) (mean
1183 ±SD; n=4 embryos/stage; Mann-Whitney). **I.** Quantification of velocity magnitudes from data in (A).
1184 Note attenuated velocity at E15.5 (mean ±SD; n=4 embryos/stage; Linear Mixed-Effects model.

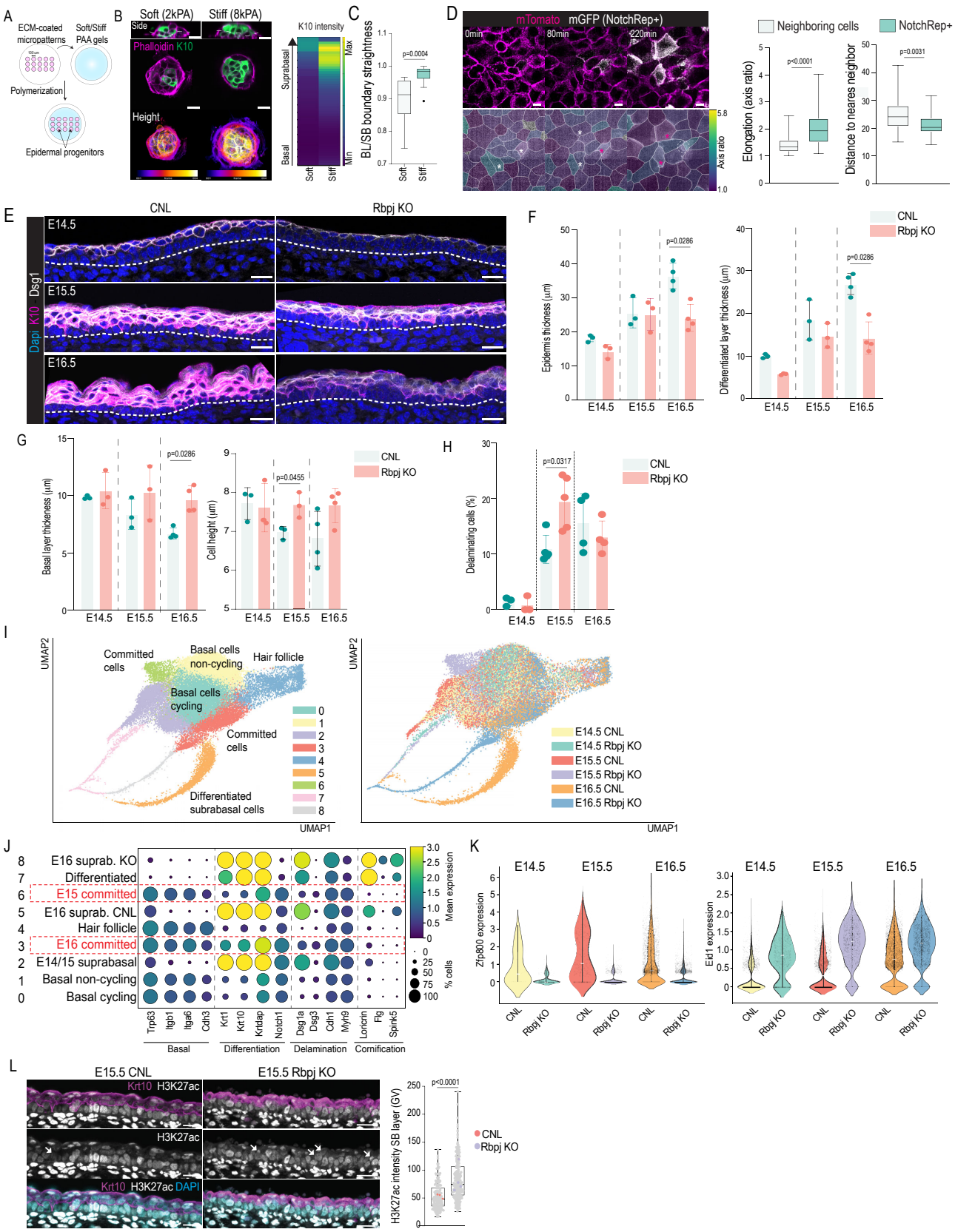

Figure 6. Tissue rigidity and cell shape changes drive Notch- delamination and control of tissue crowding

1188 **A.** Schematic illustration of micropatterning of soft and stiff polyacrylamide (PAA) hydrogels. **B.**
1189 Representative images of primary epidermal progenitors stained with K10 (green) and phalloidin
1190 (magenta) cultured on 100-µm-diameter micropatterns on 2.5 kPa (soft) or 8 kPa (stiff) PAA gels.
1191 K10 mean intensity was quantified as a function of the distance from the bottom of the micropatterns.
1192 Note the increased K10 mean intensity in the suprabasal region on stiff substrates. **C.** Quantification
1193 of boundary straightness between the basal layer (bottom) and the first suprabasal layer (upper layer).
1194 (Tukey's box and whiskers, n= 10 (soft); 15 (stiff) patterns pooled across 3 independent experiments;
1195 Mann-Whitney). **D.** Representative snapshots and quantification of live imaging movies from
1196 epidermal progenitor cell monolayers from mTomato/mGFP-Cre reporter mice crossed with Notch1-
1197 ICD-Cre to detect cells that activate Notch (mGFP+). Note increased elongation and local cell
1198 density of cells (white asterisk) that subsequently activate Notch signaling (red asterisk). Dotted
1199 circle marks delamination of Notch-Reporter-positive (NotchRep+) cell (min-max box and whiskers;
1200 n=38 Notch+ cells pooled across 3 independent experiments; Mann-Whitney; scale bars 10 µm). **E.**
1201 Representative images of tissue sections from E14.5-16.5 embryos of control and Rbpj-KO mice
1202 stained against K10 (magenta) and Desmoglein 1 (Dsg1; white) (images representative of >3
1203 embryos/stage; scale bars 20 µm). **F.** Quantification of epidermal thickness from data in (A). Note
1204 reduced total and differentiated layer thickness of Rbpj-KO epidermis at E16.5 (mean ±SD; n=3
1205 embryos/E14.5 and E15.5, 4/E16.5; Mann-Whitney). **G.** Quantification of basal layer thickness and
1206 cell height from data in (E). Note increase basal layer thickness and cell height of Rbpj-KO epidermis
1207 emerging at E15.5 (mean ±SD; n=3 embryos/E14.5 and E15.5, 4/E16.5; Mann-Whitney). **H.**
1208 Quantification of delaminating cells from data in (E). Note increase in delaminating cells in Rbpj-KO
1209 epidermis at E15.5 (mean ±SD; n=3 (E14.5), 5 (E15.5), 4 (E16.5) embryos; Mann-Whitney). **I.**
1210 UMAP representation of the Leiden clusters (left panel) and biological samples (right panel) of
1211 filtered epidermal cells from scRNAseq. **J.** Dotplot of selected genes across E14.5-E16.5 epidermal
1212 cells. Clusters 3 and 6 (in red) represent committed basal cell populations enriched in Rbpj-KO cells
1213 of E15.5 and E16.5 embryos. **K.** Violin plots of Zfp800 of Eid1 expression across E14.5-E16.5 in
1214 control and Rbpj-KO epidermal cells. **L.** Representative images and H3K27ac nuclear intensity
1215 quantification from tissue sections from E15.5 embryos of control and Rbpj-KO mice stained for
1216 H3K27ac (grey), K10 (magenta) and DAPI (cyan) (n= 176 (CNL), 234 (Rbpj-KO) cells pooled
1217 across 3 (CNL) /4 (Rbpj-KO) embryos; Student's t-test; Scale bars 20 µm).

1218

Supplementary Figures

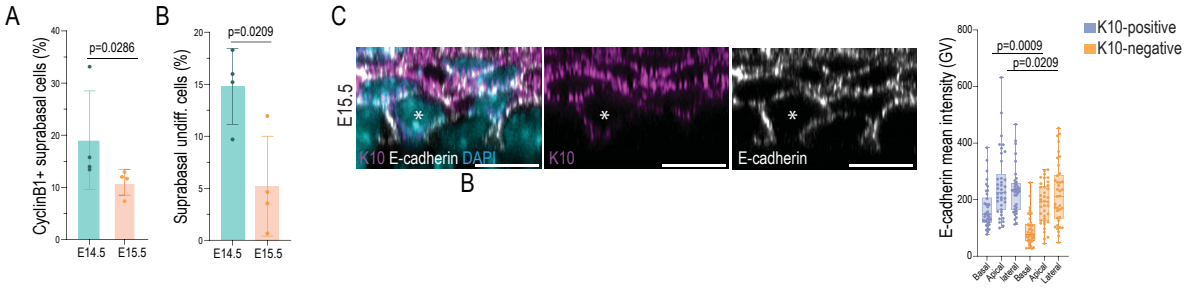

Supplementary Figure 1.

A. Quantification of differentiated (K10-positive) CyclinB1+ cells in the suprabasal layer (mean ±SD; n=4 embryos /stage; Mann-Whitney) **B.** Representative images and quantification of delaminating cells in E15.5 embryo from 3D whole mounts stained against E-cadherin, K10 and DAPI. Delaminating cell is marked with a white asterisk; scale bars 10 µm; min-max box and whiskers; n=38 cells pooled across 3 embryos; Friedman/Dunn's).

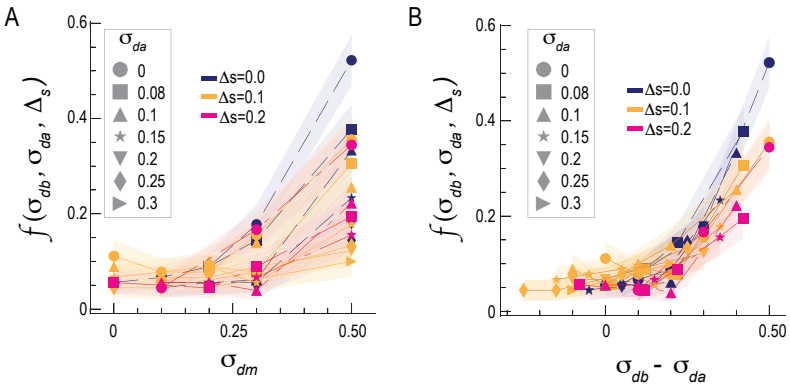

Supplementary Figure 2. Systematic quantification of delamination rates as a function of the properties of the delaminating and stiffness of the surrounding tissue Δ*s*

A. Uncollapsed delamination rates. **B.** Delamination rates plotted as a function of $\sigma_{db} - \sigma_{da}$, which do not fully collapse, indicating that an additional energetic contribution is required. Figure 2D in the main text shows that adding the term $c\,\Delta s$leads to a collapse of the curves onto a single master curve as a function of $\sigma_{db} - \sigma_{da} + c\,\Delta s$.

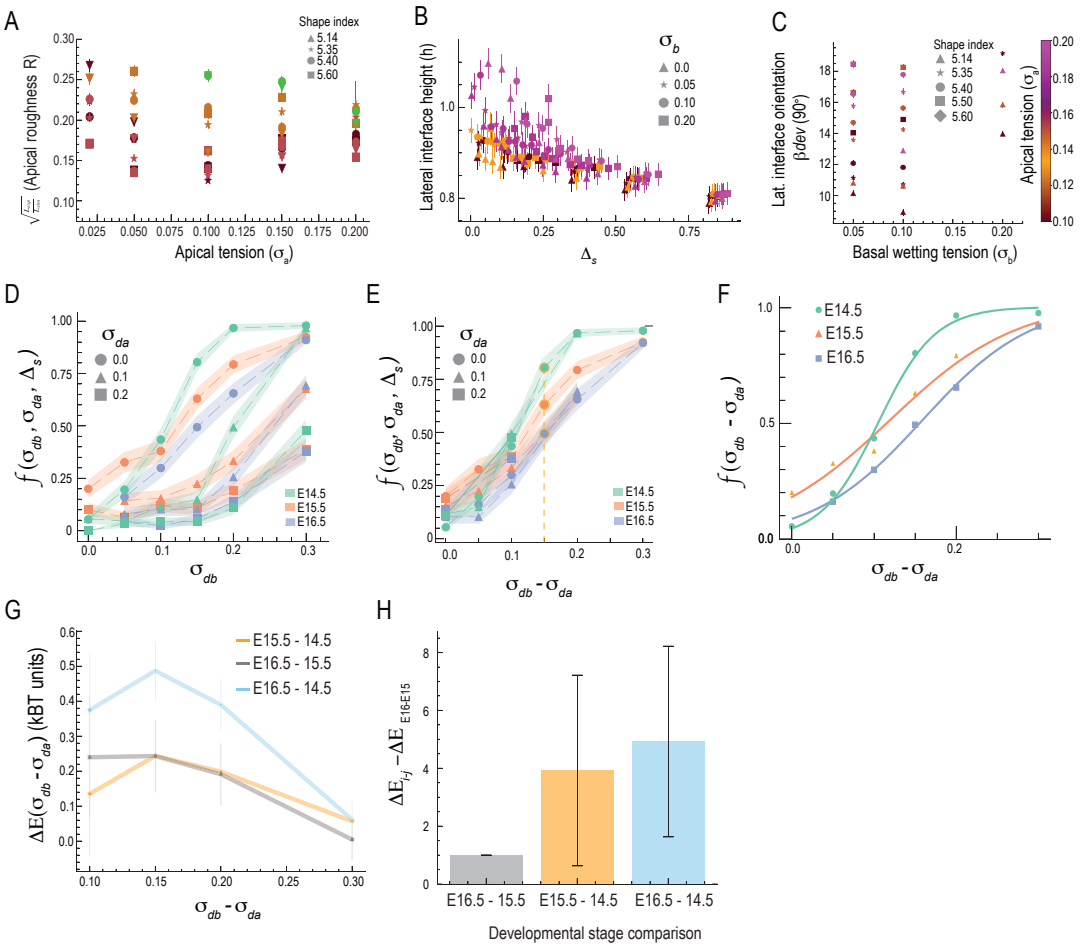

Supplementary Figure 3. Geometric observables for mechanical barrier and quantification of delamination rates and associated energy barriers as function of delaminating cell properties. **A-C.** Uncollapsed plots of basal-suprabasal interface roughness, basal cell lateral interface height, and lateral interface orientation, respectively, measured in the 3D model simulations across mechanical parameter space ($\sigma_a, \sigma_b, \Delta s$). Corresponding collapsed plots are shown in main Fig. 3G, I, K. **D.** Quantification of delamination rates data as function of the delaminating cell tensions (σ_{db}, σ_{da}) parameter space. **E.** Data from (F) collapses as a function of $\sigma_{db} - \sigma_{da}$. **F.** Curve fits to the collapsed delamination rate data shown in panel (B) across the developmental stages. **G.** Quantification of the differences in energy barriers between developmental stages as a function of the differences in delaminating cell properties (σ_{da}, σ_{db}). **H.** Normalized averages (normalized by the energy barrier difference between stages E16 and E15) of the differences in energy barriers between stages E15.5 and E14.5, and between E16.5 and E14.5, plotted as a function of $\sigma_{db} - \sigma_{da}$.

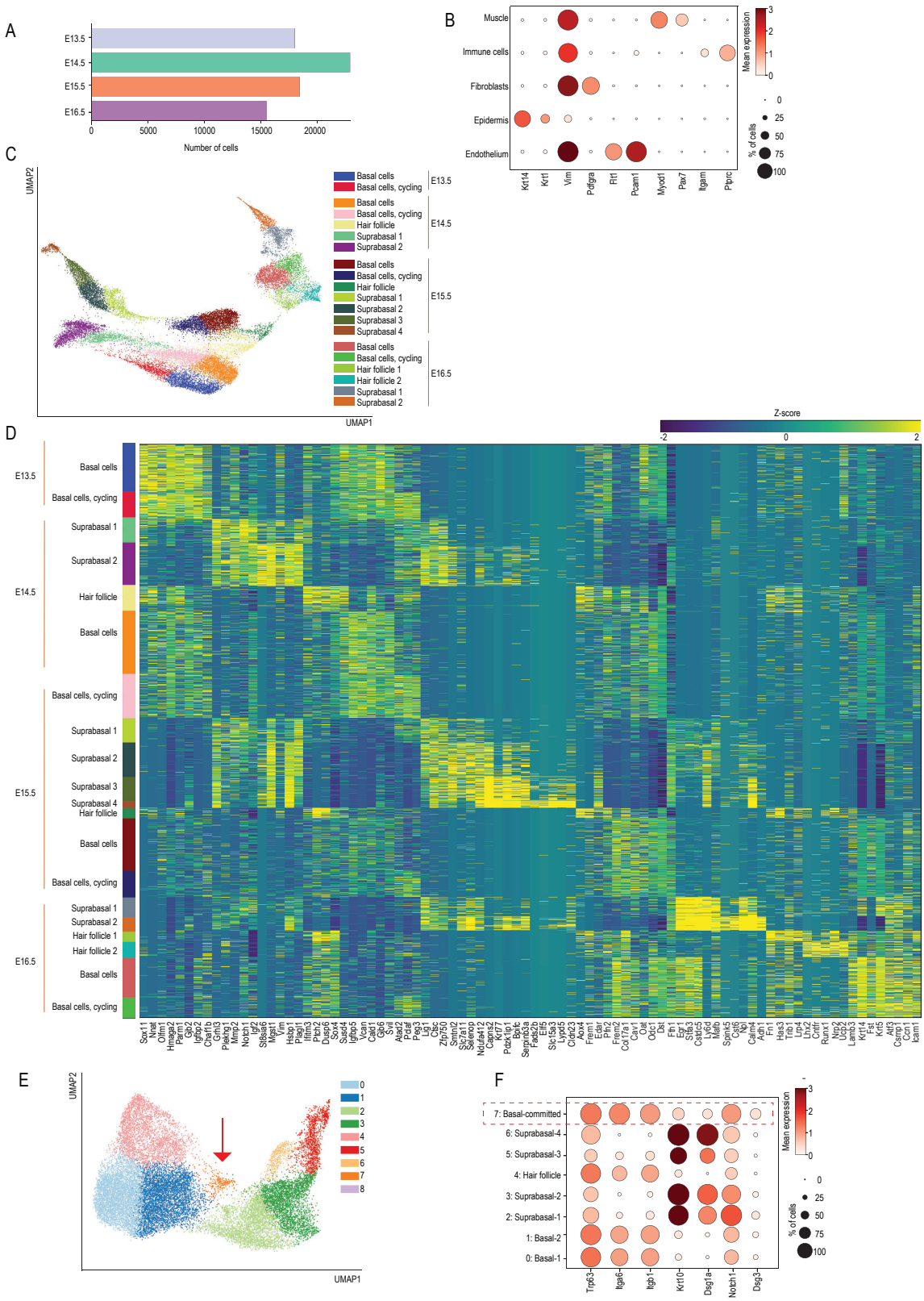

Supplementary Figure 4.

A. Bar plot showing number of sequenced cells/genotype. **B.** Dot plot of selected key cell type-specific marker genes across annotated cell types. **C.** UMAP visualization of Leiden clusters of

epidermal cells with main cell states annotated. **D.** Heatmap of marker genes for epidermal Leiden clusters. **E.** UMAP visualization of Harmony integrated epidermal cells. Red arrow indicates committed cell population. **F.** Dot plot of selected key cell type-specific marker genes across annotated cell types from Harmony integrated epidermal cells. Red dotted rectangle indicates committed cell population.

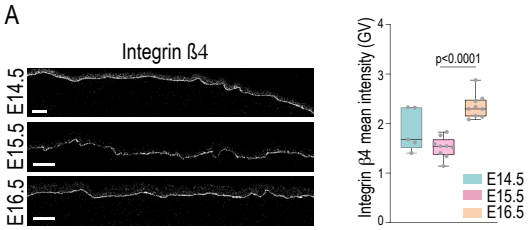

Supplementary Figure 5.

A. Representative images and quantifications of tissue sections from E14.5- 16.5 embryos analyzed by mass cytometry. Note increased expression of integrin β4 (mean ±SD; scale bars 50 µm; n=3 embryos/stage; Two-way ANOVA/Tukey's.

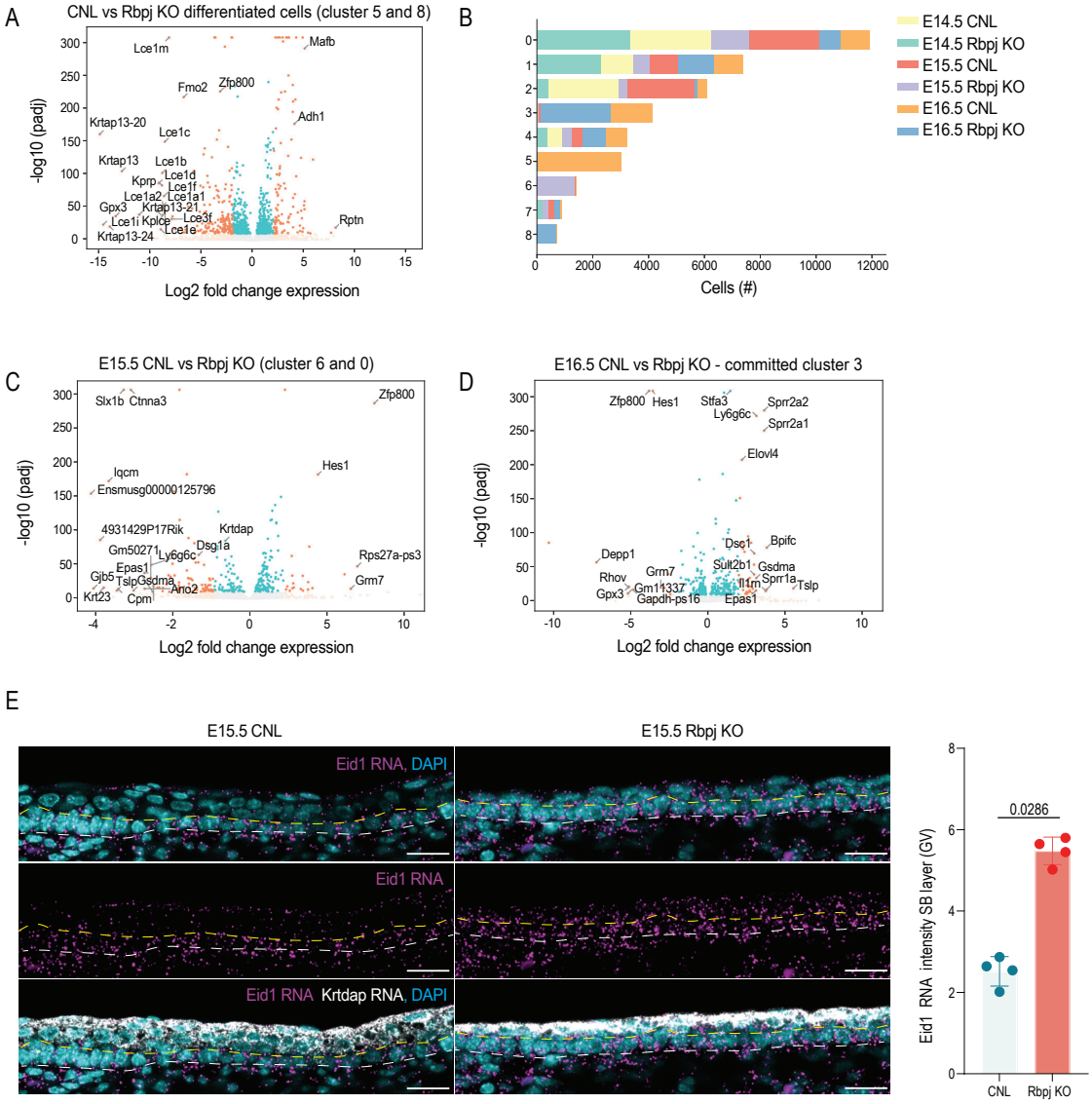

Supplementary Figure 6.

A. Volcano plot showing differentially expressed genes between Rbpj-KO and CNL epidermis from differentiated cell clusters 5 and 8. **B.** Bar plot showing number of sequenced cells/embryonic stage and genotype across Leiden clusters. **C.** Volcano plot showing differentially expressed genes between E15.5 Rbpj-KO and CNL epidermis from clusters 6 and 0. **D.** Volcano plot showing differentially expressed genes between E16.5 Rbpj-KO and CNL epidermis from cluster 3. **E.** Representative images and quantification of tissue sections from E15.5 embryos of control and Rbpj-KO mice of the expression of Eid1 (magenta) and Keratin-dap (grey) detected by RNA in situ hybridization. Dotted lines mark basal layer (n=4 embryos/condition; Mann-Whitney). Scale bars 20 µm.